https://doi.org/10.5194/bg-2021-207
Preprint. Discussion started: 3 August 2021

Biogeosciences Discussions
Open Access
EGU

A seamless ensemble-based reconstruction of surface ocean pCO_2 and air–sea CO_2 fluxes over the global coastal and open oceans

Thi Tuyet Trang Chau, Marion Gehlen, and Frédéric Chevallier

Laboratoire des Sciences du Climat et de l'Environnement, LSCE/IPSL, CEA-CNRS-UVSQ, Université Paris-Saclay, F-91191 Gif-sur-Yvette, France

Correspondence: Thi Tuyet Trang Chau (trang.chau@lsce.ipsl.fr)

Abstract. We have estimated the air–sea CO_2 fluxes ($fgCO_2$) over the global ocean from the open sea to the continental shelves. Fluxes and associated uncertainty were computed from an ensemble-based reconstruction of CO_2 sea surface partial pressure (pCO_2) maps trained with observations from the Surface Ocean CO_2 Atlas v2020 database. The ensemble mean (which is the best estimate provided by the approach) fits independent data well and a broad agreement between the spatial distribution of model-data differences and the ensemble standard deviations (which are our model uncertainty estimate) is seen. The space-time varying uncertainty fields identify oceanic regions where improvements in data reconstruction and extensions of the observational network are needed. Poor reconstructions of pCO_2 are primarily found over the coasts and/or in regions with sparse observations, while $fgCO_2$ estimates with largest uncertainty are observed over the open Southern Ocean ($44°S$ southward), the subpolar regions, the Indian gyre, and upwelling systems.

Our estimate of the global net sink for the period 1985–2019 is $1.643 \pm 0.125\,\mathrm{PgC\,yr^{-1}}$ including $0.150 \pm 0.010\,\mathrm{PgC\,yr^{-1}}$ for the coastal net sink. Results suggest that the open ocean Subtropical Pacific (between 18°N–49°N) has the strongest CO_2 sink ($0.485 \pm 0.014\,\mathrm{PgC\,yr^{-1}}$) among the basins of the world, followed by the open ocean sub-basins in the Southern hemisphere. The coastal Subpolar Atlantic (between 49°N–76°N) is the most significant coastal net sink, amounting to one third of the total coastal uptake; the northern Pacific continental shelves (north of 18°N) are the next contributors. The Equatorial Pacific (between 18°S–18°N) is the predominant source emitting $0.523 \pm 0.016\,\mathrm{PgC\,yr^{-1}}$ of CO_2 back to the atmosphere. Based on the mean flux density per unit area, the most intense CO_2 drawdown is, however, observed over the Arctic (76°N poleward) followed by the Subpolar Atlantic and Subtropical Pacific for both open ocean and coastal sectors. The mean efflux density over the Equatorial Pacific remains the highest, but similar densities can also be found along other strong upwelling systems in the equatorial band.

https://doi.org/10.5194/bg-2021-207
Preprint. Discussion started: 3 August 2021


Biogeosciences Discussions Open Access EGU

1 Introduction

Since the onset of the Industrial Era, humankind has profoundly modified the global carbon (C) cycle. The use of fossil fuels, cement production, and land use change has added 700 ± 75 PgC (best estimate $\pm 1\sigma$) to the atmosphere between 1750 and 2019 (Friedlingstein et al., 2020). An estimated 285 ± 5 PgC of this excess C stayed there, the remainder was taken up by the ocean (170 ± 20 PgC) and the land biosphere (230 ± 60 PgC). While the fraction of total CO_2 emissions sequestered by the ocean remained rather stable ($22 - 25\%$) over the past six decades (Friedlingstein et al., 2020), the global ocean sink has varied significantly at interannual time scales (Rödenbeck et al., 2015). Global ocean biogeochemical models (GOBMs) are used within the framework of the annual assessment of the global carbon budget (Friedlingstein et al., 2020) to annually re-estimate the means and variations of CO_2 sinks and sources over the global ocean and major basins. However, these recent model-based estimates need to be benchmarked against observation-based estimates in order to better understand the global carbon budget as well as its yearly re-distribution in the biosphere (Hauck et al., 2020).

In situ measurements of sea surface fugacity of CO_2 collected by an international coordinated effort of the ocean observation community and combined into the Surface Ocean CO_2 Atlas (SOCAT, https://www.socat.info/, Bakker et al., 2016) provide an observational constraint on the assessment of the ocean C sinks and sources. Despite an increasing number of observations since the 1990s, data density remains uneven in space and time. While, for instance, data coverage is sparse over the Southern basins of the Atlantic and Pacific oceans, observations are seasonally biased towards the summers at high latitudes (Landschützer et al., 2014; Denvil-Sommer et al., 2019; Gregor et al., 2019).

Various data-based approaches including machine learning, classical regression, and mixed layer schemes have been proposed in Rödenbeck et al. (2013); Landschützer et al. (2014, 2016); Denvil-Sommer et al. (2019); Bushinsky et al. (2019); Gregor et al. (2019); Watson et al. (2020); Denvil-Sommer et al. (2021) (see also other mapping methods in Rödenbeck et al., 2015) to infer gridded maps of surface ocean pCO_2 from the sparse set of observations, targeting the improved reconstruction of spatially and temporally varying surface pCO_2 fields and air–sea CO_2 fluxes over the global ocean and major basins. While these studies provide model bias and standard errors and use these statistics as model uncertainty estimates, none has so far analysed space-time varying uncertainty estimates, e.g., based on the model dispersion of a large set of realizations of pCO_2 and air–sea flux estimates. Moreover, up to recently, most of these reconstructions did not cover the coastal ocean, a gap that has been closed by validated estimates of mean climatologies of pCO_2 (Laruelle et al., 2017; Landschützer et al., 2020), air–sea flux density and the total coastal C sink (Laruelle et al., 2014).

In this work, we first propose a new inference strategy for this problem based on an ensemble of 100 neural network models mapping the monthly gridded SOCATv2020 data. The approach consists in reconstructing the monthly pCO_2 fields and the contemporary air–sea fluxes over the period 1985–2019 on a spatial resolution of $1^\circ \times 1^\circ$. Mean and standard deviation are computed from the ensembles of 100 model outputs. They are used to estimate the mean state and uncertainty of the carbon fields seamlessly for different time scales (e.g., monthly, yearly, and multi-decadal) and spatial scales (e.g., grid cells, sub-basins, and the global ocean). Based on the uncertainty estimates, we identify regions that should be prioritized in future observational programs and model development in order to reduce model errors and uncertainty. Potential drivers of the spatio-temporal

https://doi.org/10.5194/bg-2021-207
Preprint. Discussion started: 3 August 2021

distribution and the magnitude of air–sea CO_2 fluxes are discussed with the aim to better attribute underlying processes and detect potential focus regions for further studies on the evolution of oceanic CO_2 sources and sinks.

2 Methods

2.1 General formulation

The air–sea flux density $(\mathrm{molC\,m^{-2}yr^{-1}})$ is calculated here by the standard bulk equation

$$\begin{aligned} fg\mathrm{CO_2} &= Tr\ \Delta p\mathrm{CO_2} \\ &= kL\,(1-f_{\mathrm{ice}})\left(p\mathrm{CO_2^{atm}} - p\mathrm{CO_2}\right), \end{aligned} \tag{1}$$

where k is the gas transfer velocity computed as a function of the 10-meter wind speed following Wanninkhof (2014), L is the temperature-dependent solubility of CO_2 (Weiss, 1974), f_{ice} and $p\mathrm{CO_2^{atm}}$ are, respectively, the sea ice fraction and the atmospheric CO_2 partial pressure. In Eq. (1), a positive (negative) flux indicates oceanic CO_2 uptake (release). Details and references for the source of these variables are given in Table S1, except for $p\mathrm{CO_2}$ that is described in the following section.

2.2 An ensemble-based approach for the reconstruction of sea surface $p\mathrm{CO_2}$ and air–sea $\mathrm{CO_2}$ fluxes

The partial pressure of CO_2 in Eq. (1) is estimated monthly over each point of the global ocean by analysing sparse in situ $p\mathrm{CO_2}$ measurements, gathered and gridded at monthly and 1-degree resolution in the 2020 release of the Surface Ocean CO_2 Atlas (SOCAT, https://www.socat.info/). SOCATv2020 covers the period 1985–2019. We have regressed these $p\mathrm{CO_2}$ values against a set of predictors with a non-linear function, a feed-forward neural network model (FFNN), as illustrated in Fig. 1. Our predictors are biological, chemical, and physical variables commonly associated with the variations of $p\mathrm{CO_2}$ (e.g., Landschützer et al., 2013; Denvil-Sommer et al., 2019; Gregor et al., 2019): sea surface height (SSH), sea surface temperature (SST), sea surface salinity (SSS), mixed layer depth (MLD), chlorophyll-a (CHL), atmospheric CO_2 mole fraction ($x\mathrm{CO_2}$). A $p\mathrm{CO_2}$ climatology (Takahashi et al., 2009) and the geographical coordinates (latitude and longitude) were also added to the predictors. Table S1 details the data source. All data were reprocessed and co-located at the same SOCAT resolution following Denvil-Sommer et al. (2019).

An ensemble of 100 FFNNs was used to reconstruct monthly $p\mathrm{CO_2}$ fields with a $1^\circ \times 1^\circ$ resolution over the global surface ocean during years 1985–2019. This ensemble approach was developed at the Laboratoire des Sciences du Climat et de l'Environnement (LSCE) as both an extension and an improvement of the first version (LSCE-FFNN-v1, Denvil-Sommer et al., 2019). Our model outputs are part of the Copernicus Marine Environment Monitoring Service (CMEMS). Throughout the paper, it is hence referred to as CMEMS-LSCE-FFNN.

To reconstruct the $p\mathrm{CO_2}$ fields over the global ocean for each target month over the 1985–2019 period, all the available SOCAT data and the co-located predictors have been collected for the month before and the month after the target month. We randomly extracted two thirds of each one of these datasets to make training datasets for the FFNNs, leaving the remaining

https://doi.org/10.5194/bg-2021-207
Preprint. Discussion started: 3 August 2021

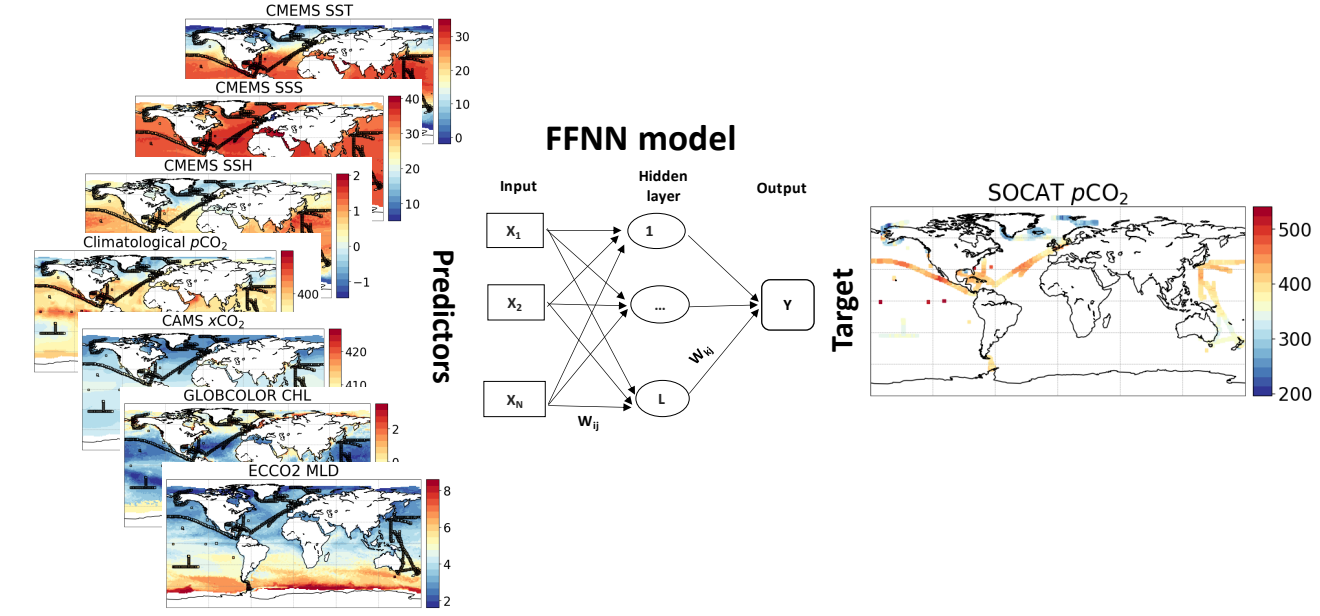

Figure 1. Illustration of a feed-forward neural network (FFNN) model mapping monthly SOCAT observations and feature variables (Table S1) co-located at a spatial resolution of $1^\circ \times 1^\circ$.

third to be corresponding test datasets. The FFNNs were then trained for each target month. The random extraction and the FFNN training were repeated 100 times so that 100 versions of the monthly FFNNs have been obtained. The exclusion of the reconstructed month itself in the training and test datasets follows a leave-p-out cross-validation approach, where p is the number of SOCAT observations in the target month. This approach allows to reduce model over-fitting, as well as to assess the quality of the reconstruction against SOCAT data that are fully independent from the training phase. Equation (1) was then applied to the ensembles of FFNN outputs of pCO_2 in order to obtain ensembles of monthly global $fgCO_2$ fields.

2.3 Coastal and regional division

The reconstructed pCO_2 fields and air–sea CO_2 fluxes are analysed over the global ocean, at particular locations, and in 11 oceanic sub-basins used by the Regional Carbon Cycle Assessment Project Tier 1 (RECCAP1, Canadell et al., 2011) and previous studies (Schuster et al., 2013; Sarma et al., 2013; Ishii et al., 2014; Lenton et al., 2013; Wanninkhof et al., 2013; Landschützer et al., 2014). In order to distinguish the coastal from the open ocean, we use the coastal mask from the MARgins and CATchments Segmentation (MARCATS, Laruelle et al., 2013) interpolated on the $1^\circ \times 1^\circ$ SOCAT grid. Details of the regional (open and coastal) division are given in Table 1 and Fig. 2.

With the above definitions, the coastal regions encompass 6.33% of a total maximum ocean area of 352.77×10^6 km^2. The computation of these numbers was based on the maximum data coverage of the CMEMS-LSCE-FFNN reconstruction taking into account the variable monthly sea–ice fraction. The number of SOCATv2020 observations used in the reconstruction of

https://doi.org/10.5194/bg-2021-207
Preprint. Discussion started: 3 August 2021

Biogeosciences Discussions Open Access EGU

Table 1. Indication of 11 RECCAP1 regions (Fig. 2). Only the total area with respect to the maximum coverage of the reconstructed data is accounted for each region.

Index	Region	Latitude	Area (10^6km^2)	
			Open ocean	Coast
	Globe (G)	90°S – 90°N	330.42	22.35
1	Arctic (Ar)	76°N – 90°N	1.07	0.99
2	Subpolar Atlantic (SpA)	49°N – 76°N	8.88	4.15
3	Subpolar Pacific (SpP)	49°N – 76°N	6.16	3.65
4	Subtropical Atlantic (StA)	18°N – 49°N	23.22	1.83
5	Subtropical Pacific (StP)	18°N – 49°N	36.37	1.65
6	Equatorial Atlantic (EA)	18°S – 18°N	23.15	1.05
7	Equatorial Pacific (EP)	18°S – 18°N	66.50	3.22
8	South Atlantic (SA)	44°S – 18°S	17.79	0.83
9	South Pacific (SP)	44°S – 18°S	37.15	0.50
10	Indian Ocean (IO)	44°S – 30°N	52.80	2.71
11	Southern Ocean (SO)	90°S – 44°S	59.47	3.12

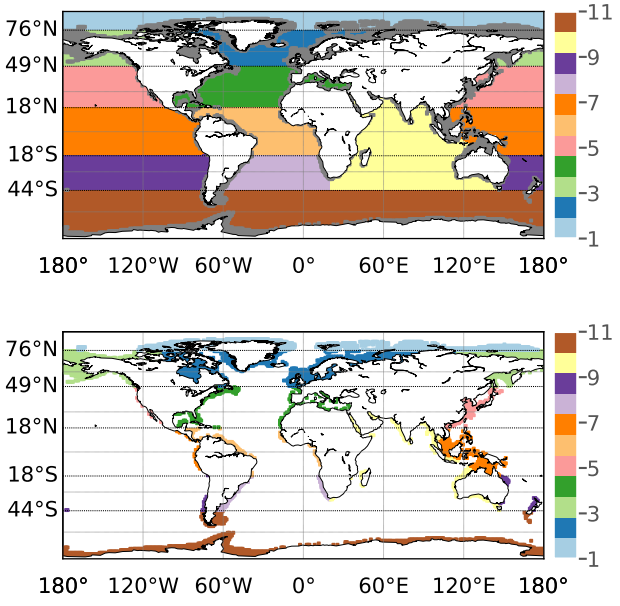

Figure 2. Map of RECCAP1 regions (Regional Carbon Cycle Assessment and Processes, Canadell et al., 2011) and MARCATS coastal mask (MARgins and CATchments Segmentation, Laruelle et al., 2013) co-located on the $1° \times 1°$ SOCAT grid.

pCO_2 is reported in Table S2 for each region, with 301,449 in total and 10.36% of the data observed over the predefined coastal regions.

https://doi.org/10.5194/bg-2021-207
Preprint. Discussion started: 3 August 2021

2.4 Statistics

The mean and standard deviation of the 100-member ensembles of pCO_2 and $fgCO_2$ are respectively chosen as their best estimate and the associated uncertainty ($\sigma_{\mathrm{ensemble}}$). Uncertainty statistics are computed from the ensemble at each desired space-time resolution. For air–sea fluxes, the unit of a best estimate and its 1-sigma uncertainty is $\mathrm{mol C\,m^{-2}yr^{-1}}$ for a flux density and converted to $\mathrm{PgC\,yr^{-1}}$ for an integral over a region or the global ocean.

Model robustness is also evaluated on SOCAT observations and the reconstructed pCO_2 fields. Standard statistics include the coefficient of determination (r^2) and the root-mean-square deviation (RMSD) with

$$\begin{aligned}\mathrm{MSD}\left(pCO_2^{\mathrm{Reconstruction}},\, pCO_2^{\mathrm{Observation}}\right) = &\left[\mathrm{Mean}\left(pCO_2^{\mathrm{Reconstruction}} - pCO_2^{\mathrm{Observation}}\right)\right]^2 \\ &+ \left[\mathrm{Std}\left(pCO_2^{\mathrm{Reconstruction}} - pCO_2^{\mathrm{Observation}}\right)\right]^2. \qquad (2)\end{aligned}$$

Misfit mean (model bias) and misfit standard deviation (denoted as σ_{misfit} hereafter) involved in Eq. (2) are also used for model evaluation. All these scores are computed for different coastal and open regions from the scale of grid cells to the global scale. Note that r^2, RMSD, misfit mean, and σ_{misfit} reflect the model performance with respect to observations, while $\sigma_{\mathrm{ensemble}}$ measures the stability of the model best estimate. Nevertheless, these different statistics should consistently reflect the skill of the model reconstruction, e.g., depending on the density and distribution of data sampling.

3 Results

3.1 Evaluation

To verify the robustness of the mapping method, we first evaluate the goodness of fit of reconstructed pCO_2 against the independent SOCAT observations from the leave-p-out cross-validation set (see Sect. 2.2).

Empirical Cumulative Distribution Functions (CDFs) and frequency histograms drawn from these data are compared in Figs. 3a and 3b. While a frequency histogram in Fig. 3a shows the number of pCO_2 data at SOCAT observation location distributed for each bin, the one in Fig. 3b (grey) reflects how the pCO_2 values at observation location are distributed within their bounds. The probability–probability (P–P) plot of Fig. 3b (blue curve) measures the fit in the distributions of the reconstruction and SOCAT data. The same presentation is used in Figs. 3c and 3d for the misfit standard deviation σ_{misfit} and the ensemble standard deviation $\sigma_{\mathrm{ensemble}}$ at SOCAT observation location (see their values in Figs. S2c and S2g).

The reconstructed pCO_2 field matches SOCAT data well: both are normally distributed with the same mean of $361.3\ \mu\mathrm{atm}$ (Fig. 3a) and a high agreement for all percentiles (Fig. 3b) is seen. The slight under- or overestimation at high and low percentiles implies that the model is slightly biased towards the mean value, as is expected when predictor variables do not fully explain predictand variables in the training dataset. This reduced variability is also reflected in the difference between the data standard deviation based on SOCAT pCO_2 ($41.79\ \mu\mathrm{atm}$) and the one based on CMEMS-LSCE-FFNN ($36.30\ \mu\mathrm{atm}$).

Displayed on Fig. 3c, both misfit standard deviation (σ_{misfit}) and model uncertainty ($\sigma_{\mathrm{ensemble}}$) empirically follow the exponential distribution. σ_{misfit} is much higher than $\sigma_{\mathrm{ensemble}}$ as the CDF and frequency histogram of the former (blue) show

https://doi.org/10.5194/bg-2021-207
Preprint. Discussion started: 3 August 2021

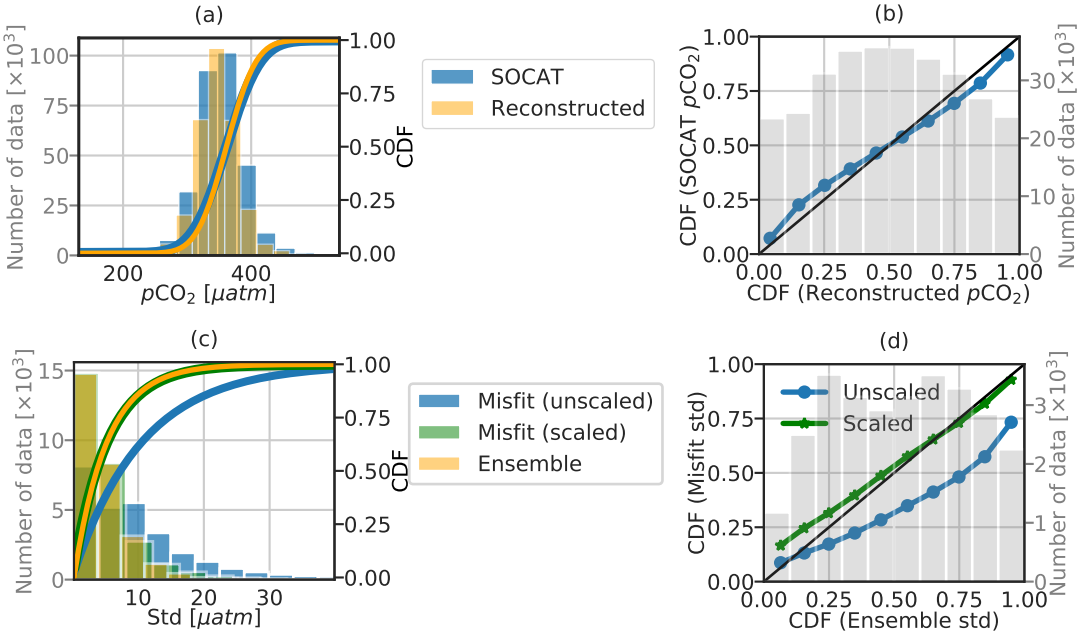

Figure 3. Comparison between empirical Cumulative Distribution Functions (CDFs) of (a,b) SOCATv2020 data and the reconstructed pCO_2 field and (c,d) model–observation misfit standard deviation (std) and model uncertainty, as seen in Fig. S2. In (c,d), the distribution of misfit std values scaled with a factor of 2 is plotted. A histogram with the axis in grey of the four subplots displays the number of data distributed in each bin, the bins with less than 200 data for (a) and 20 data for (c) have been excluded. In (b,d), the bisector is shown in black.

heavier tails than those of the latter (orange), which brings the P–P curve below the bisector in Fig. 3d. When dividing the misfit standard deviation values shown in Fig. S2c by 2, σ_{misfit} (green) shares a similar distribution as $\sigma_{\mathrm{ensemble}}$ (orange). A natural explanation for this twofold tuning factor would point to a simple lack of spread of the ensemble, either because the FFNN ensemble would be too small or because the uncertainty in the predictors (not accounted for here in the ensemble) would be significant. The SOCAT CO_2 fugacity data are sampled at uneven space-time resolution (e.g., the sampling frequency varies between one read per minute to one per hour). Gridded data correspond to the average of measurements collected within a $1° \times 1°$ box and in a month over the entire cell area. Variability in the number of cruises and analytical equipment induces measurement latitude and longitude offsets from the cell center, e.g., with an average of $0.34° \pm 0.14°$ as reported in Sabine et al. (2013) which are not taken into account.

Assume that

(1) Such practical imperfection presents a systematic error in each measurement from the true data with an overall standard deviation of $\sigma_{\mathrm{observation}}$.

https://doi.org/10.5194/bg-2021-207
Preprint. Discussion started: 3 August 2021

(2) Systematic errors between SOCAT observations and the reconstructed data equal those between the true data and the reconstructed data.

As observation errors are independent from the random errors induced by the ensemble approach in each grid cell (further to the implementation of the leave-p-out cross-validation in model training; see Sect. 2.2), σ_{misfit} in Eq. (2) can be interpreted as

$$\sigma^2_{\mathrm{misfit}} = \sigma^2_{\mathrm{ensemble}} + \sigma^2_{\mathrm{observation}}, \tag{3}$$

where $\sigma^2_{\mathrm{observation}}$ varies in space and time and is larger near shelves (see the observation variability in Figs. S1b and S1c).

The interpretation of the magnitude of mismatch is therefore not straightforward, but we note that the spatial distribution of model errors and uncertainty estimates over the global ocean (Fig. 5) consistently identifies the spatial distribution of the model skill. This asset is prioritized in our preliminary study and further analysed in the next sections. The twofold factor used for the illustration in Fig. 3 has not been kept for the following results.

3.1.1 Global ocean

At global scale, the model fits the data with a mean bias close to zero, an RMSD of $20.48\ \mu\mathrm{atm}$, and a coefficient of determination (r^2) of 0.76. The temporal fluctuation of the spatial mean of the model–observation mean difference over the global ocean is displayed on Fig. 4a along with the number of observations. The time series of the yearly bias (black curve) starts with a large positive value ($7.47 \pm 1.60\ \mu\mathrm{atm}$) in year 1985 ($\sim 740$ observations). The bias drops during the following years and fluctuates around zero from 1994 onward (the number of observations per year is generally larger than 5000). In general, the magnitudes of the yearly model bias and model spread are correlated with the number of observations which increased greatly since the 1990s. The importance of sustained data coverage is emphasized by Fig. S3. It illustrates the fact that large model–observation mismatches are frequently associated with the interruption of Voluntary Observing Ship (VOS) lines and thus with the tracking of CO_2 fugacity over large regions. The larger bias computed prior to the 1990s (Fig. 4a) might intuitively lead to the conclusion that model outputs are less reliable than those in the later periods. However, this global mean score is influenced by the amount and distribution of data, and consequently the increased observation density does not fully explain the reconstruction skill. For instance, even with a higher number of observations than that in the pre-1990s, years 2001 and 2007 stand out with strong negative biases (-5.44 ± 1.26 and $-3.12 \pm 0.92\ \mu\mathrm{atm}$, respectively). While such a comparison between the global bias and the number of observations highlights the lack of a simple relationship between the number of data and the skill of the mapping method, the ensemble spread (dark grey area) of model errors, representing the spread of the annual mean of $p\mathrm{CO}_2$ estimates at SOCAT observation location, is reduced with an exponential decay constant of 0.46 ± 0.06 per 1000 observations (Fig. 4b).

The model scores for the open ocean over the period 1985 to 2019 are $17.87\ \mu\mathrm{atm}$ for RMSD and 0.78 for r^2. The skill of this novel method, which uses only two thirds of SOCAT data for fitting each of 100 FFNN models ranks similar to those from alternative statistical reconstruction approaches (Rödenbeck et al., 2013; Landschützer et al., 2014; Gregor et al., 2019) which have been used to complement model-based estimates of the ocean carbon sink (Friedlingstein et al., 2019, 2020).

https://doi.org/10.5194/bg-2021-207
Preprint. Discussion started: 3 August 2021

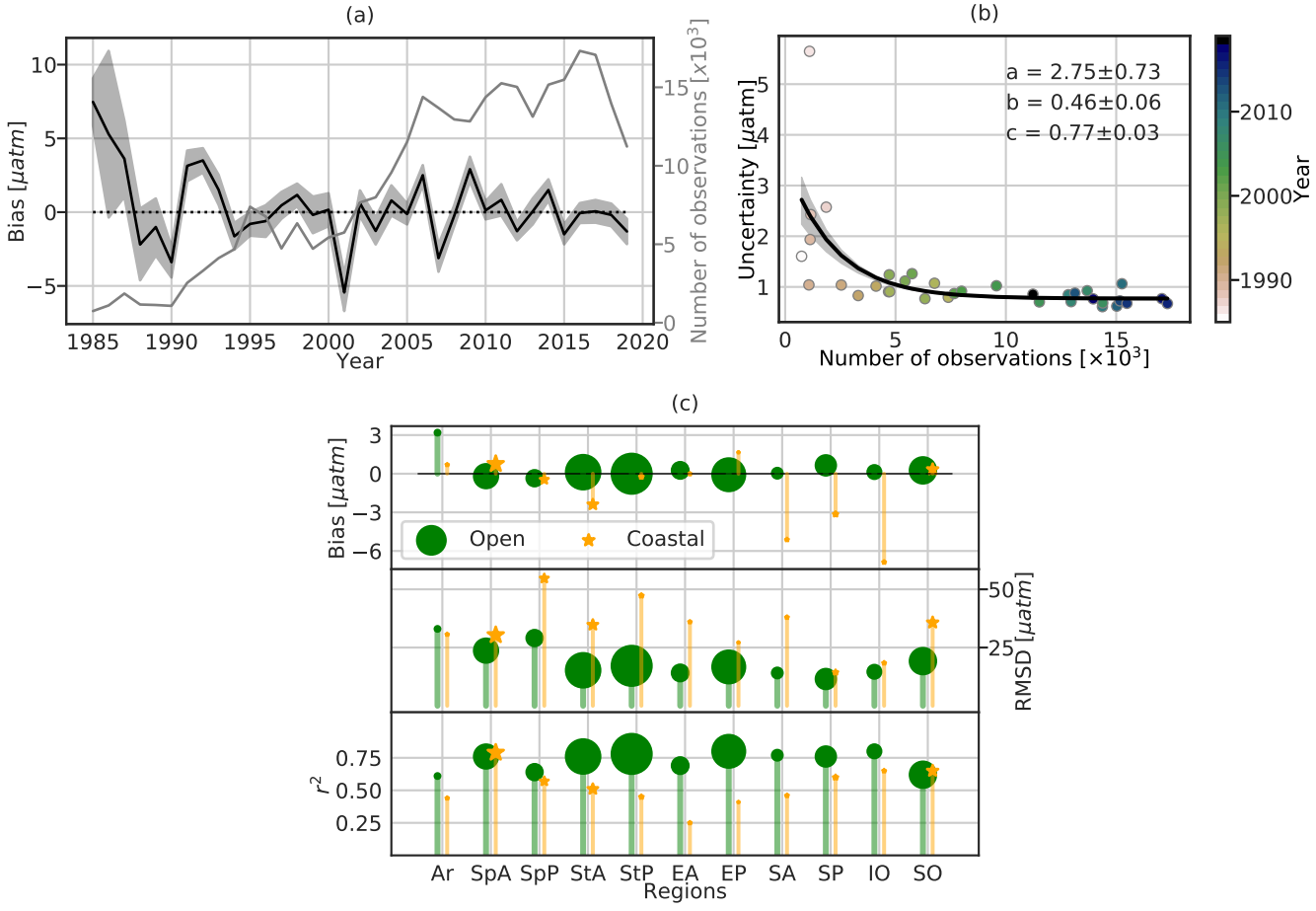

Figure 4. (a) Timeseries of the yearly mean model bias, i.e., the reconstructed pCO_2 data minus SOCATv2020 data, over the global ocean. The black curve and dark grey area represent the mean estimate and 1σ-envelop of errors of the 100-member ensemble, the light grey curve represents the total number of observations used in the FFNN model construction. (b) Exponential fits of the model uncertainty (the magnitude of the 1σ-envelop in Fig. 4a) against the number of yearly SOCAT observations. The exponential function is $y = a\exp^{-bx} + c$. The black curve is derived from the best fit and the grey shaded area corresponds to the spread derived from standard errors of parameter estimates. (c) Statistical scores for 11 oceanic regions with the size of each scattered object proportional to the number of regional observations (Table S2).

The CMEMS-LSCE-FFNN reconstruction over the coastal regions for the full period is roughly twice less effective than over the open ocean in terms of RMSD ($35.86\ \mu$atm) while it shows a rather good fit with $r^2 = 0.70$. The high RMSD reflects local high model errors along the continental shelves (Fig. S2). For the 1998–2015 period, the CMEMS-LSCE-FFNN model scored an RMSD of $35.84\ \mu$atm, larger than the coastal reconstruction error of $26.8\ \mu$atm by Landschützer et al. (2020). The latter unified data for the same period from two conceptually equivalent reconstruction models, one covering the open ocean (Landschützer et al., 2016) and one targeting the coastal ocean (Laruelle et al., 2017). Besides, Landschützer et al. (2020) used

https://doi.org/10.5194/bg-2021-207
Preprint. Discussion started: 3 August 2021

the coastal reconstruction by Laruelle et al. (2017) with a finer spatial resolution and a broader definition of the continental shelf (400 km distance from the sea shore and a $0.25° \times 0.25°$ resolution) than CMEMS-LSCE-FFNN. However, coastal reconstruction errors remain high despite the increase in spatial resolution and in the number of observations. Coastal and shelf seas are characterized by complex physical and biological dynamics leading to high variability at small scales. For instance, $p\mathrm{CO}_2$ levels over the Californian shelf can exceed 850 μatm and with a spatial gradient of $p\mathrm{CO}_2$ as large as 470 μatm over a distance less than 0.5 km (Chavez et al., 2018; Feely et al., 2008). Clearly, further model improvement is needed in order to capture such high spatial and temporal variability of surface ocean $p\mathrm{CO}_2$ present in observations (see also in Bakker et al., 2016; Laruelle et al., 2017, and references therein).

In the following subsections, we present and discuss the reconstruction skills for different ocean regions, as well as for open ocean and coastal domains (Fig. 4c). Complete results including the numbers of observations, RMSDs, and r^2 for each region are summarized in Table S2.

3.1.2 Arctic

Data coverage is particularly sparse over the Arctic ocean (Ar) with 50 to 220 samples per year since 2007 and an interruption in 2010 (Fig. S3). While continental shelves account for 50% of the region's area, only one third of the observations are from coastal regions. Moreover, observations are seasonally biased towards ice-free summer months (Bakker et al., 2016). Though reconstruction standard errors are similar for open basins and coastal regions (RMSDs of 33.01 and 30.65 μatm respectively), the coefficient of determination is higher over the open ocean (r^2= 0.61) compared to coastal seas (r^2= 0.44), suggesting a higher model skill over open basins. The close-to-zero bias of the coastal reconstruction shown in Fig. 4c results from the compensation between highly positive and negative values over the continental shelves of Alaska, the Canadian Archipelagos, the Barents and Kara Seas (see Fig. S2), the yearly bias fluctuates within $[-50, 30]$ μatm (Fig. S3). Of all open ocean regions, the Arctic reconstruction has the highest bias (3.19 μatm). Cold Arctic waters are characterized by low levels of surface ocean $p\mathrm{CO}_2$ due to the temperature effect on CO_2 solubility and the seasonal draw-down of dissolved inorganic carbon (DIC) during summer months by intense biological production (Feely et al., 2001; Takahashi et al., 2009; Arrigo et al., 2010). Assuming that the Arctic predictors remain within the range of global relationships, the overestimation of $p\mathrm{CO}_2$ by CMEMS-LSCE-FFNN, as seen in Fig. 4c, suggests a possible underestimation of biological productivity. While the preceding remains conjectural, we acknowledge a large uncertainty on the contribution of biological activity (net primary production, NPP) on surface ocean $p\mathrm{CO}_2$, as it is "proxied" by chlorophyll-a derived from remote sensing (Maritorena et al., 2010; Babin et al., 2015b). Overall, these scores point to the Arctic as a relatively poorly reconstructed region.

3.1.3 Atlantic

The North Atlantic stands out as a region with high data coverage (Fig. S1a) and a rapidly increasing number of data since 2000 (Fig. S3). A sustained sampling effort adds between 2000 to 4000 data each year to the database over the Subtropical (StA) and Subpolar Atlantic (SpA) regions (including between $10 - 40\%$ of coastal observations). The data density over the

https://doi.org/10.5194/bg-2021-207
Preprint. Discussion started: 3 August 2021


Biogeosciences Discussions Open Access EGU

North Atlantic stands in strong contrast to the often less than 1000 observations per year collected over the Equatorial (EA) and South Atlantic (SA) and their strong year-to-year variability.

The comparison between the reconstructed open ocean pCO_2 and independent observations over the four sub-regions of the open Atlantic (Fig. 4c and Table S2) reveals small mean model–observation differences, which together with the two other scores, identify the Atlantic as the basin with the highest reconstruction skill. RMSDs corresponding to the StA, the EA, and the SA are below 15.50 μatm and r^2 values are in the range of $[0.69, 0.77]$. While a larger RMSD is obtained over the SpA (23.68 μatm), the r^2 of 0.76 falls close to the upper end of the range determined for the three other regions. As discussed in Schuster et al. (2013), large temporal and spatial gradients of pCO_2 as well as its variability driven by a diversity of physical and biological processes (e.g., surface ocean temperature gradients, biological production, vertical mixing, and horizontal advection of water masses) keep the analysis of pCO_2 over the SpA challenging.

Despite accounting for over 59% of the total of coastal observations, skillful data reconstruction over the coastal Atlantic regions remains difficult. RMSDs are in general above 30 μatm and, with the exception of the coastal SpA ($r^2 = 0.79$), below 51% of the observed variance is predicted by the model over the other regions (StA: 0.51, EA: 0.25, SA: 0.46). The large model–observation mismatch along the Atlantic continental shelves (Fig. S2) reflects the poor reconstruction of pCO_2 over regions under the influence of upwelling systems (e.g., Moroccan coast, Benguela), large river discharges (e.g., Amazon, Congo, Florida, Mississippi), and the bottle necks of gulfs or bays (e.g., Bahamas, English Channel).

3.1.4 Pacific

With the exception of the Subpolar Pacific (SpP), the number of observations has increased regularly over the Pacific basin. In the recent years, from 1000 to 3500 observations are recorded per year over the Subtropical Pacific (StP), the Equatorial Pacific (EP), and the South Pacific (SP) (Fig. S3). Forty percent of open ocean observations are collected over the StP and the EP in the years 1985–2019. Corresponding RMSDs are 17.15 and 16.68 μatm, with r^2 above 0.78. Despite a data coverage below one third of that reported for the two previous regions, the model proved skillful in reconstructing pCO_2 over the SP (Fig. 4c) with RMSD $= 11.50$ μatm and $r^2 = 0.76$.

The overall good performance of the FFNN over these three Pacific sub-regions contrasts with its lack of skill over the open SpP. The observation density is poor and highly variable. Before 1994, less than 250 observations per year are available to constrain the reconstruction, followed by several years of intense effort and a maximum of about 1250 observations in 2000, before decreasing again to the pre-1994 values. At first order, skill scores fluctuate in line with observation density. During the first period (up to 1994), the bias varies within $[-25, 25]$ μatm (Fig. S3), it decreases close to $[-2, 4]$ μatm between 1997 and 2000, and increases again along with decreasing data density. Much like the SpA, the SpP is a region characterized by a strong spatial and temporal variability in pCO_2 (Ishii et al., 2014), challenging any reconstruction method. The difficulty is further aggravated by the paucity of data in this region compared to the SpA. Skill scores are modest over the SpP with an RMSD of 29.08 μatm and r^2 of 0.64 (Fig. 4c and Table S2).

The ratio between coastal and open ocean observations is $1:24$. The paucity of observations for the coastal domain is reflected by lower skill scores compared to the open ocean. Over the coastal SpP, for example, the RMSD amounts to 54.69 μatm,

https://doi.org/10.5194/bg-2021-207
Preprint. Discussion started: 3 August 2021


Biogeosciences Discussions Open Access EGU

while it is $29.08\ \mu\mathrm{atm}$ for the corresponding open ocean region. Comparable to the SpP, data reconstruction over the coastal regions of the StP (e.g., North American coast, Sea of Japan), as well as over the western EP (e.g., Peruvian upwelling) and the SP (e.g., offshore Chile) remains difficult (Fig. S2). Similar results have been found by Landschützer et al. (2020).

The EP is characterized by strong equatorial upwelling making it one of the major outgassing regions of $\mathrm{CO_2}$ (Feely et al., 2001). Surface ocean $p\mathrm{CO_2}$ shows a strong interannual variability predominantly in response to the El Niño Southern Oscillation (ENSO), the dominant regional climate mode (Rödenbeck et al., 2015; Landschützer et al., 2016; Denvil-Sommer et al., 2019). Before the 2000s, negative [positive] peaks of bias (Fig. S3) coincide with La Niña years; e.g., 1988–1990, 1995–1996, 1999–2001 [El Niño; e.g., 1986–1987, 1991–1992, 1997–1998] (see the ENSO events highlighted in Fig. 9). A strong negative bias is again computed in 2010–2012 which could reflect the lack of data during that cooling phase. On the contrary, the reconstruction seems less sensitive to the strong warm anomalies associated with the 2015–2016 El Niño. The model appears to be more efficient at reconstructing surface ocean $p\mathrm{CO_2}$ during the hot climate mode (El Niño) than during the cool one (La Niña) when enhanced upwelling drives surface ocean $p\mathrm{CO_2}$ up and towards unusual large values. This allows us to anticipate the effect of a general decrease in data collection during 2020–2021 in response to the Coronavirus disease 2019 (COVID-19) pandemic on the estimation of the ocean carbon sink. We expect a high negative bias in model estimates of $p\mathrm{CO_2}$ and the consequent underestimation of $\mathrm{CO_2}$ outgassing due to the combined impact of Covid19 on data collection and La Niña conditions governing since August/September 2020 (https://public.wmo.int/en/media/press-release/la-nina-has-developed). It is worthwhile to also note that observations in the eastern EP have declined in the last five years compared to the other years in the 2010s.

3.1.5 Indian Ocean

The Indian Ocean (IO) is the third largest oceanic regions by area but also the one with the lowest data density. With the exception of the year 1995 (approximately 1900 observations), as few as 500 data have been collected per year (Fig. S3), yielding a total number of observations often below 10 per grid cell for the entire reconstruction period (Fig. S1a). There have been even less than 75 observations per year over the continental shelf. However, the reconstruction over the coastal region is comparable to the open IO with a low RMSD ($< 19\ \mu\mathrm{atm}$) and a high correlation to the observations ($r^2 = 0.65$). The overall negative bias shown in Fig. 4c for the coastal IO points to the model underestimating coastal $p\mathrm{CO_2}$ levels. Large errors are distributed along the western Arabian Sea, the western Madagascar, and the tropical eastern IO (Fig. S2). These regions are under the influence of the southwest monsoon giving rise to a seasonal upwelling regime (see Feely et al., 2001; Sabine et al., 2002; Sarma et al., 2013, and references therein). Strong seasonal upwelling results in a marked seasonal cycle of surface ocean $p\mathrm{CO_2}$ with high levels during the upwelling season. The paucity of data is likely to limit the skill of the model reconstruction of the seasonal cycle over large parts of the IO with consequences for the annual mean analyzed here.

3.1.6 Southern Ocean

Up to recently, data coverage over the Southern Ocean (SO) has been sparse (Fig. S1a), irregular at grid cell scale, and biased towards Austral summer months (e.g. Bushinsky et al., 2019; Gregor et al., 2019). A strong sampling effort allowed a recent

https://doi.org/10.5194/bg-2021-207
Preprint. Discussion started: 3 August 2021

increase in observations to reach up to 2000 observations per year (Fig. S3). Model scores for the open, respectively the coastal ocean are: RMSDs of 19.18 μatm and 35.73 μatm, as well as r^2 of 0.62 and 0.65. The reconstruction lacks skill over the continental shelves of South America and Antarctica (see Fig. S2).

In general, the pCO_2 reconstruction over the SO has less skill compared to the Atlantic or the Pacific due to the paucity in observations compared to its large area. Rödenbeck et al. (2015) reported inconsistent reconstructed interannual variability of pCO_2 between different data-based methods. The interannual variability is large due to the natural variability of the coupled ocean-atmosphere system characterized by one of the globe's strongest ocean current, strong winds, vertical mixing and upwelling of DIC rich deep waters (Gregor et al., 2018; Gruber et al., 2019). Efforts to improve pCO_2 reconstruction are ongoing and include model development (e.g., Gregor et al., 2017), as well as the increase in data coverage by the addition of data from different sampling platforms (e.g., profiling floats, Bushinsky et al., 2019). For the time being, CMEMS-LSCE-FFNN stands out as one of the most skillful models with respect to observations in the SO (Friedlingstein et al., 2019, 2020; Hauck et al., 2020).

3.2 Long term mean and uncertainty estimates

Fig. 5 shows temporal mean estimates, their associated uncertainty, and RMSDs of the monthly air–sea pCO_2 gradient (ΔpCO_2) and CO_2 fluxes ($fgCO_2$) over the full period (see also Fig. S4 for the coastal regions only). In the top maps, the regions in red are dominant CO_2 uptake regions (influxes) and the regions in blue are dominant source regions of CO_2 to the atmosphere (effluxes). The uncertainty of ΔpCO_2 is merely computed from the ensemble of the reconstructed sea surface pCO_2 since the randomness in the atmospheric pCO_2 field is assumed to be negligible. Due to impacts of wind stress, solubility of CO_2, and seasonal sea–ice coverage on the gas transfer coefficient, spatial distributions of mean estimates, their uncertainty, and RMSDs of ΔpCO_2 (Figs. 5a, 5c, 5e) and $fgCO_2$ (Figs. 5b, 5d, 5f) differ from low to high values. The means of air–sea fluxes integrated/averaged over different RECCAP1 regions (Table 1) are shown in Fig. 6. The distribution of uncertainty estimates and number of observations for these regions is also displayed on Fig. 7, wherein only values smaller than 90%-quantile of uncertainty estimates shown in Figs. 5c and 5d are plotted to reduce the effects of outliers on data visualization. The seasonal average computed over the full reconstruction period of air–sea CO_2 fluxes over the global ocean is shown in Fig. 8.

3.2.1 Arctic

The Arctic ocean stands out as the region with the strongest CO_2 uptake per unit area with 2.336 ± 0.104 molC m^{-2}yr^{-1} for the open sea and 1.522 ± 0.108 molC m^{-2}yr^{-1} for the continental shelf margins (Figs. 5b and 6b). At the scale of grid cells, air–sea gradients of pCO_2 are large but the downward fluxes are relatively modest over the shelves of the eastern Greenland, the Barents and Kara Seas, and the Siberia Seas (Fig. 5 or S4). During the sea–ice covered seasons, these coastal regions are neutral while the open ocean Arctic sectors (e.g., the Norwegian Sea, the Barents Sea, the Kara Seas) are CO_2 sinks with moderate influx densities (Fig. 8). The open ocean influx density exceeds 3 molC m^{-2}yr^{-1} in the Arctic summer. This substantial amount of CO_2 uptake is driven by low surface ocean temperature, seasonal changes in sea–ice cover, and intense biological production. Increasing light availability and input of nutrients through melt waters and river discharges sustain high levels of

https://doi.org/10.5194/bg-2021-207
Preprint. Discussion started: 3 August 2021

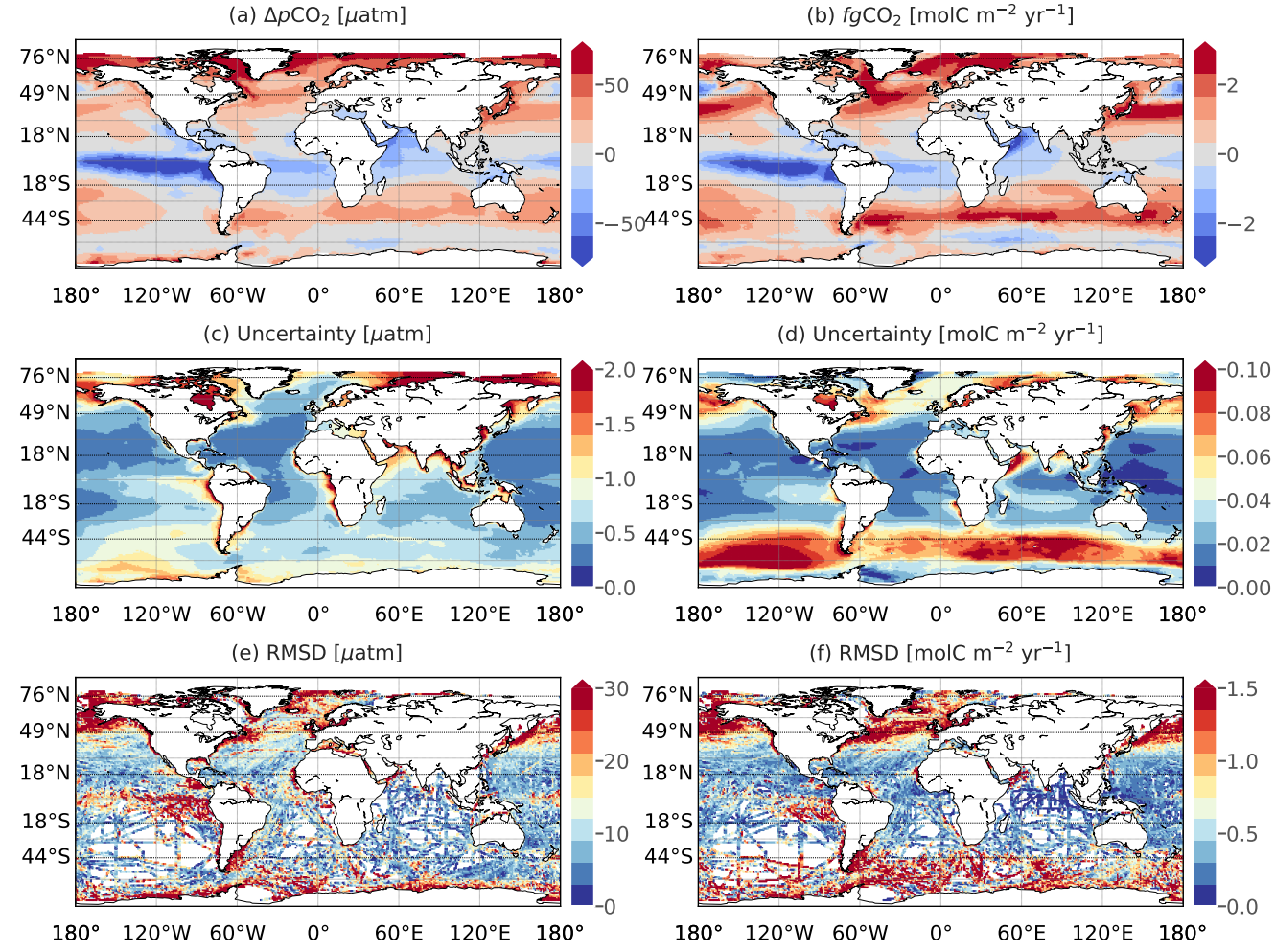

Figure 5. Climatological mean (top) and uncertainty (middle) of air–sea pCO_2 difference (a, c) and of CO_2 fluxes (b, d) over 1985–2019. Uncertainty is computed as the standard deviation of the 100-member CMEMS-LSCE-FFNN model outputs of sea surface pCO_2 and air–sea CO_2 fluxes. The bottom plots (e, f) show RMSDs between the SOCAT data (or data-based estimates of fluxes for (f)) and the mean CMEMS-LSCE-FFNN model outputs.

315 primary production and CO_2 drawdown (Bates and Mathis, 2009; Arrigo et al., 2010; Yasunaka et al., 2016). Notwithstanding, the Arctic ocean represents roughly 0.58% of the total surface ocean area (Table 1) and the yearly mean CO_2 uptake integrated over the Arctic for the full period amounts to only 1.64% of the global ocean sink (Table 2 and Fig. 6a).

3.2.2 Atlantic

The open ocean Subpolar Atlantic (SpA) sink contributes approximately 78% to the total SpA annual C uptake (0.259 ± 0.011 320 $\mathrm{PgC\,yr^{-1}}$), as well as with 12.29% to the total ocean sink (1.643 ± 0.125 $\mathrm{PgC\,yr^{-1}}$, Table 2). Per unit area, the open ocean

https://doi.org/10.5194/bg-2021-207
Preprint. Discussion started: 3 August 2021

Biogeosciences Discussions Open Access EGU

Table 2. Yearly mean of contemporary air–sea CO_2 fluxes ($PgC\,yr^{-1}$) integrated over the global ocean and 11 RECCAP1 regions. Mean estimate (ensemble mean) $\pm$ uncertainty (ensemble std) of the CMEMS-LSCE-FFNN approach is shown for the coast (C), the open ocean (O), and the total area (T). For a comparison, estimates derived from RECCAP1 (Canadell et al., 2011; Schuster et al., 2013; Ishii et al., 2014; Sarma et al., 2013; Lenton et al., 2013; Wanninkhof et al., 2013) are provided. In column 'RECCAP1', values in parentheses are the 'best' estimates proposed by RECCAP1 studies, the others are the estimates computed with different methods using pCO_2 observations. With an exception for the global estimate* (Wanninkhof et al., 2013), those of the RECCAP1 sub-basins are available only for the open ocean.

Approach		CMEMS-LSCE-FFNN		RECCAP1
Regions		1985–2019	1990–2009	
Globe	(T)	1.643 ± 0.125	1.486 ± 0.114	
	(O)	1.493 ± 0.122	1.344 ± 0.111	1.18*
	(C)	0.150 ± 0.010	0.141 ± 0.009	0.18*
Arctic (Ar)	(T)	0.027 ± 0.001	0.024 ± 0.001	
	(O)	0.016 ± 0.001	0.015 ± 0.001	(0.12 ± 0.06)
	(C)	0.011 ± 0.001	0.010 ± 0.001	
Subpolar Atlantic (SpA)	(T)	0.259 ± 0.011	0.255 ± 0.010	$0.07 \pm 0.04, 0.30 \pm 0.13$
	(O)	0.202 ± 0.009	0.197 ± 0.008	(0.21 ± 0.06)
	(C)	0.057 ± 0.004	0.058 ± 0.004	
Subtropical Atlantic (StA)	(T)	0.214 ± 0.011	0.202 ± 0.009	$0.18 \pm 0.09, 0.24 \pm 0.16$
	(O)	0.204 ± 0.010	0.192 ± 0.009	(0.26 ± 0.06)
	(C)	0.010 ± 0.001	0.010 ± 0.001	
Equatorial Atlantic (EA)	(T)	-0.117 ± 0.009	-0.128 ± 0.008	$-0.10 \pm 0.05, -0.12 \pm 0.14$
	(O)	-0.113 ± 0.009	-0.123 ± 0.008	(-0.12 ± 0.04)
	(C)	-0.004 ± 0.001	-0.004 ± 0.001	
South Atlantic (SA)	(T)	0.192 ± 0.016	0.174 ± 0.015	$0.25 \pm 0.12, 0.21 \pm 0.23$
	(O)	0.184 ± 0.015	0.167 ± 0.015	(0.14 ± 0.04)
	(C)	0.008 ± 0.001	0.007 ± 0.001	
Subpolar Pacific (SpP)	(T)	0.040 ± 0.010	0.029 ± 0.009	$0.44 \pm 0.21, 0.37$
	(O)	0.008 ± 0.008	-0.002 ± 0.007	(0.47 ± 0.13)
	(C)	0.032 ± 0.004	0.031 ± 0.003	
Subtropical Pacific (StP)	(T)	0.523 ± 0.016	0.512 ± 0.014	
	(O)	0.495 ± 0.015	0.485 ± 0.014	
	(C)	0.028 ± 0.003	0.027 ± 0.002	
Equatorial Pacific (EP)	(T)	-0.503 ± 0.022	-0.514 ± 0.020	$-0.51 \pm 0.24, -0.27$
	(O)	-0.490 ± 0.021	-0.500 ± 0.020	(-0.44 ± 0.14)
	(C)	-0.013 ± 0.003	-0.013 ± 0.003	
South Pacific (SP)	(T)	0.358 ± 0.029	0.343 ± 0.029	$0.29 \pm 0.14, 0.24$
	(O)	0.352 ± 0.029	0.337 ± 0.028	(0.37 ± 0.08)
	(C)	0.006 ± 0.0004	0.006 ± 0.0004	
Indian Ocean (IO)	(T)	0.300 ± 0.033	0.281 ± 0.027	0.24 ± 0.12
	(O)	0.305 ± 0.033	0.286 ± 0.027	(0.37 ± 0.06)
	(C)	-0.004 ± 0.002	-0.005 ± 0.002	
Southern Ocean (SO)	(T)	0.349 ± 0.070	0.307 ± 0.061	0.27 ± 0.13
	(O)	0.330 ± 0.069	0.290 ± 0.061	(0.42 ± 0.07)
	(C)	0.018 ± 0.002	0.017 ± 0.002	

https://doi.org/10.5194/bg-2021-207
Preprint. Discussion started: 3 August 2021

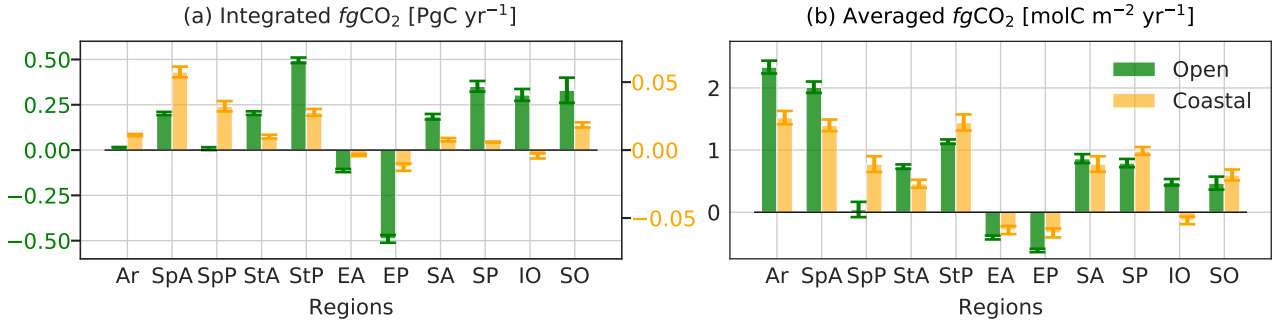

Figure 6. Distribution of contemporary fluxes (positive into the ocean) over 11 regions (see in Fig. 2) for the full period 1985–2019. Uncertainties of the mean estimates of air–sea fluxes integrated (a) or averaged (b) over each region are shown with error bars.

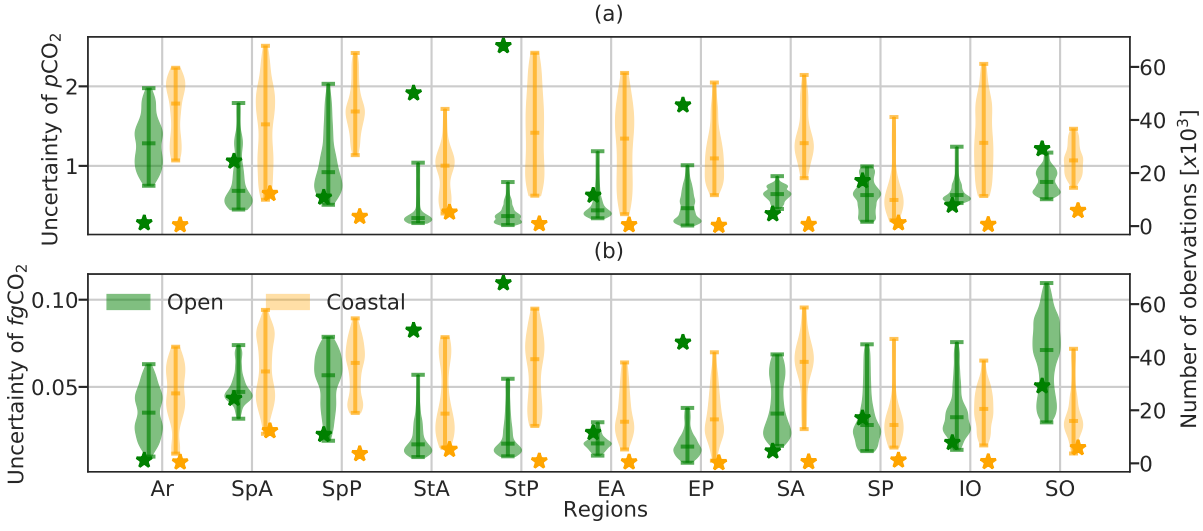

Figure 7. Distribution (violin) of all uncertainty estimates (Figs. 5c and 5d) and the total number (star) of SOCAT observations (Fig. S1a) split for 11 RECCAP1 regions. A violin plot shows the range, median, and density of uncertainty estimates for pCO_2 (μatm) and $fgCO_2$ (molC m^{-2}yr^{-1}).

influx amounts to 2.012 ± 0.092 molC m^{-2}yr^{-1}, the coastal ocean influx is 30.51% less than its open ocean counterpart and slightly lower than the coastal Arctic sink (Fig. 6b). However, when integrated over the region, the yearly uptake of 0.057 ± 0.004 PgC yr^{-1} makes the coastal SpA the strongest sink among the 11 coastal regions (Fig. 6a). The interplay between temperature- and biology driven effects results in changes in the seasonal and spatial distributions of surface ocean pCO_2 and ultimately air–sea CO_2 fluxes. During boreal winter/spring, high wind speeds enhance gas transfer velocities, contribute to a strong cooling and an increase of CO_2 solubility (Takahashi et al., 2009; Feely et al., 2001), both enhancing uptake of CO_2 over the Labrador Sea, the North Atlantic and Norwegian Currents, the Barents and Kara Seas (Fig. 8). High wind speeds

https://doi.org/10.5194/bg-2021-207
Preprint. Discussion started: 3 August 2021

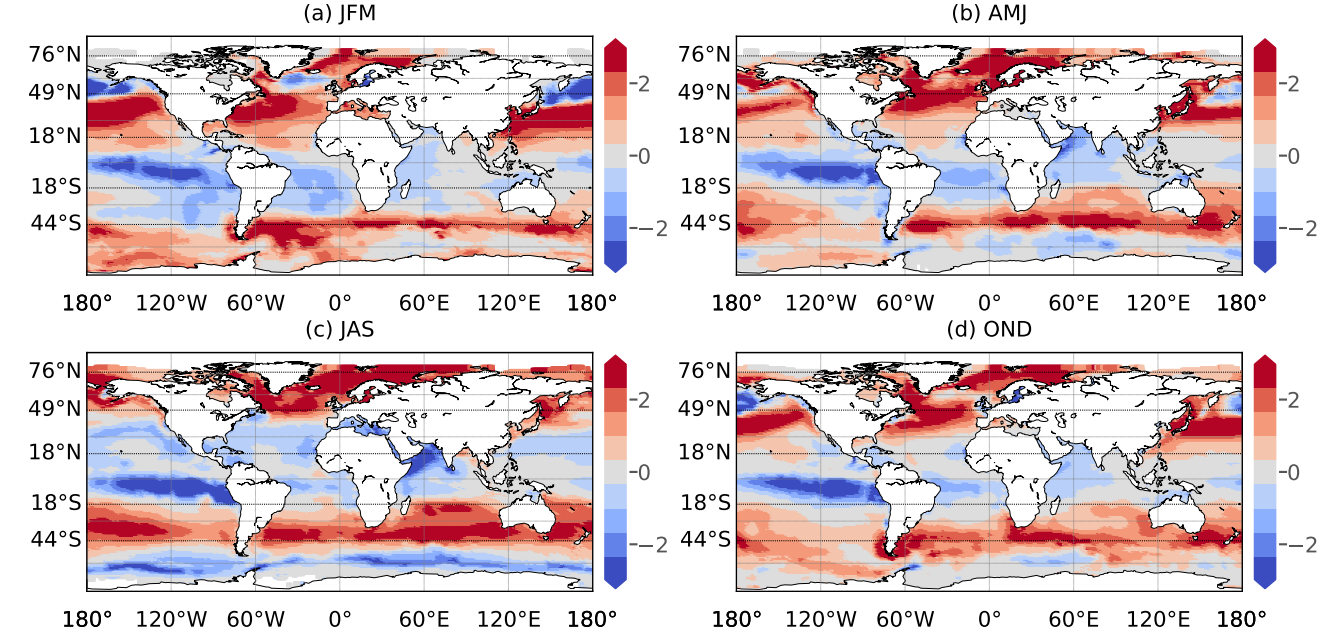

Figure 8. Seasonality of downward CO_2 fluxes [$\mathrm{molC\,m^{-2}yr^{-1}}$] in 1985–2019. Temporal means of the reconstructed $fgCO_2$ field for January to March (JFM), April to June (AMJ), July to September (JAS) and, October to December (OND) are shown.

also strengthen vertical mixing, a process supplying dissolved inorganic carbon (DIC), alkalinity (ALK), and nutrients to the surface ocean. During the spring and summer months, a vigorous biological activity (Sigman and Hain, 2012) counteracts the warming induced decrease in CO_2 solubility and increase in pCO_2 by drawing down DIC, ALK, and nutrients (Feely et al., 2001). Along the coast, inputs of fresh water (decrease in salinity and increase in CO_2 solubility) and nutrients (biological activity and DIC drawdown) combine to strengthen CO_2 uptake (Arrigo et al., 2010; Yasunaka et al., 2016; Olafsson et al., 2021).

The Subtropical Atlantic (StA) is characterized by weak to moderate mean flux densities per unit area (open: $0.733 \pm 0.036\,\mathrm{molC\,m^{-2}yr^{-1}}$, coastal: $0.457 \pm 0.064\,\mathrm{molC\,m^{-2}yr^{-1}}$). The total integrated C uptake amounts to $0.214 \pm 0.011\,\mathrm{PgC\,yr^{-1}}$, with $0.204 \pm 0.010\,\mathrm{PgC\,yr^{-1}}$ contributed by the open ocean. As for the SpA, the net uptake reflects the combined effect of cooling, mixing, and biological activity. Figures 5 and S4 show the regional distribution of sources and sinks. Regions of intense CO_2 uptake are associated with the warm Gulf Stream and its northeastward extension, the North Atlantic Drift. Strong uptake is also found over the western continental shelf where strong river discharges sustain high levels of biological productivity in particular during spring (Jamet et al., 2007; Kealoha et al., 2020). Weaker sinks or sources of CO_2 in the southwestern StA and the eastern subtropical gyre are primarily driven by high surface temperature and enhanced stratification (Schuster et al., 2013). The latter restricts the vertical supply of nutrients and limits biological production. Finally, a relatively strong source of CO_2 is found over the Canary upwelling system in summer (Fig. 8).

https://doi.org/10.5194/bg-2021-207
Preprint. Discussion started: 3 August 2021


Biogeosciences Discussions Open Access EGU

The Equatorial Atlanic (EA) stands out as the second strongest source region of CO_2 after the Equatorial Pacific (EP) with a yearly outgassing of -0.117 ± 0.009 $\mathrm{PgC\,yr^{-1}}$ (Fig. 6a). Most of CO_2 is released from the open ocean with an average efflux of -0.407 ± 0.031 $\mathrm{molC\,m^{-2}yr^{-1}}$ (Figs. 5b and 6b). This intense source of CO_2 stems from upwelling of cool and CO_2-rich waters in the eastern EA. A westward increase in outgassing is observed along with the advection of CO_2-rich waters (Schuster et al., 2013). The coastal EA regions release an average of -0.288 ± 0.064 $\mathrm{molC\,m^{-2}yr^{-1}}$ of CO_2. Over large areas, the opposing effects of primary production and high surface temperature combine to weaken the coastal sink or seasonally switch it from a weak to a moderate source (e.g., the north east EA, Caribbean Sea, Venezuelan and Guiana basins, Gulf of Guinea) (Fig. 8). The Amazon river is a notable exception. Its large discharges of fresh water, nutrients, as well as of dissolved and particulate carbon turn the coastal and adjacent shelf seas into a net sink of CO_2 (Medeiros et al., 2015; Ibánhez et al., 2015).

The South Atlantic (SA) uptake amounts to 0.192 ± 0.016 $\mathrm{PgC\,yr^{-1}}$. Regions north of $30°S$ act as weak sources or are neutral with respect to air–sea exchanges of CO_2, as opposed to regions to the South which are significant sinks of CO_2 (Fig. 5b). For the full period, densities over the open and coastal regions are, respectively, 0.862 ± 0.072 $\mathrm{molC\,m^{-2}yr^{-1}}$ and 0.776 ± 0.125 $\mathrm{molC\,m^{-2}yr^{-1}}$. Coastal regions are changing from moderate sources to sinks with increasing latitude (Fig. S4). The SA has similar seasonal dynamics as the StA with CO_2 uptake in winter and outgassing in summer (Takahashi et al., 2009; Schuster et al., 2013). During the austral winter, deep mixed layers result in cold surface waters which absorb CO_2 from the atmosphere. By contrast, warming during the summer reduces the solubility of CO_2 leading to a weak sink or even a source (Fig. 8). As explained before, biological production counteracts the effect of warming and the vigorous spring bloom contributes to the uptake south of $30°S$ (Sigman and Hain, 2012; Carvalho et al., 2020).

3.2.3 Pacific

The Subpolar Pacific (SpP) is the second smallest region by area (2.78% of the total surface ocean area) and with 0.040 ± 0.010 $\mathrm{PgC\,yr^{-1}}$ (net coastal and open oecan sinks) provides the smallest contribution to the total yearly ocean C uptake (Table 2 and Fig. 6a). The coastal ocean contributes about 0.032 ± 0.004 $\mathrm{PgC\,yr^{-1}}$ to the total yearly C uptake, making the SpP the only region for which coastal fluxes exceed open ocean fluxes. The strength of its coastal C sink ranks second among all coastal regions (Fig. 6a). Seasonal features of CO_2 fluxes are shown in Fig. 8. The SpP is ice-covered during the winter months which results in close to zero air–sea fluxes per unit area north of $60°N$ (e.g., Beaufort, Siberia, and Chukchi Seas). Besides, vertical convection during winter brings up DIC-rich old waters leading to CO_2 outgassing exceeding -3 $\mathrm{molC\,m^{-2}yr^{-1}}$ in the South of the region (Bates and Mathis, 2009; Arrigo et al., 2010; Ishii et al., 2014; Yasunaka et al., 2016). An intense biological production during the boreal summer drives an intense uptake of CO_2 over the entire SpP (Feely et al., 2001; Sigman and Hain, 2012; Ishii et al., 2014). The interplay of these two seasonal mechanisms and their opposing effects make the open SpP a weak yearly net sink (Fig. 6). The average flux density per unit area is 0.044 ± 0.123 $\mathrm{molC\,m^{-2}yr^{-1}}$ over the open ocean, much smaller than the value determined for the coastal ocean of 0.775 ± 0.127 $\mathrm{molC\,m^{-2}yr^{-1}}$ (Fig. 6b). The enhanced uptake of CO_2 by the coastal ocean compared to the open ocean results from melt water discharge and high primary production over the shelves of the Chukchi and Bering Seas and the Gulf of Alaska in the spring/summer (Yasunaka et al.,

https://doi.org/10.5194/bg-2021-207
Preprint. Discussion started: 3 August 2021

2016). In addition, the combined effects of river runoff, (i.e., freshwater fluxes and the dilution of salinity and DIC-rich waters, as well as the delivery of nutrients and the enhancement of biological productivity) surpass those of winter upwelling of DIC over the Beaufort and the East Siberia Seas (Arrigo et al., 2010).

A total mean uptake of $0.523 \pm 0.016\ \mathrm{PgC\,yr^{-1}}$ makes the Subtropical Pacific (StP) the largest sink region. The open ocean contribution dominates the regional sink with $0.495 \pm 0.015\ \mathrm{PgC\,yr^{-1}}$ (Table 2 and Fig. 6a). The corresponding mean flux density per unit area is $1.136 \pm 0.036\ \mathrm{molC\,m^{-2}yr^{-1}}$ (Fig. 6b) and makes the StP rank third after the open ocean Arctic and SpA regions. As discussed for the StA, during winter months cooling and high wind intensities along the Kuroshio and North Pacific Currents enhance the uptake of CO_2 (Takahashi et al., 2009; Ishii et al., 2014). By contrast, summer warming drives the StP towards close to neutral conditions, respectively a weak source (Fig. 8). With a yearly mean uptake of $0.028 \pm 0.003\ \mathrm{PgC\,yr^{-1}}$, the coastal StP sink becomes third in terms of intensity among the coastal sinks (Fig. 6a). The influx density is $1.444 \pm 0.130\ \mathrm{molC\,m^{-2}yr^{-1}}$. Western coastal systems and shelf seas are under the influence of the delivery of freshwater and nutrients by large river systems (Liu et al., 2014). The resulting intense biological production contributes to influx densities per unit area that are higher over the western continental shelf and seas (e.g., East China Sea, Sea of Japan) than over the California upwelling system (Figs. 5b, S4b, and 8).

The Equatorial Pacific (EP) is the strongest source region of CO_2 to the atmosphere with a yearly average efflux of $-0.490 \pm 0.021\ \mathrm{PgC\,yr^{-1}}$ from the open ocean, respectively $-0.013 \pm 0.003\ \mathrm{PgC\,yr^{-1}}$ from the continental shelves. On average per unit area, the open sea emits $-0.616 \pm 0.027\ \mathrm{molC\,m^{-2}yr^{-1}}$ of CO_2. This high rate of outgassing is a distinct feature of the EP (e.g., Feely et al., 2001; Takahashi et al., 2009; Rödenbeck et al., 2015; Landschützer et al., 2016; Denvil-Sommer et al., 2019; Landschützer et al., 2019) and is primarily due to the upwelling of DIC rich deep waters. The magnitude of CO_2 release decreases westward - from Eastern boundary upwelling (e.g., Peru, Panama) to the International Date line - in line with decreasing upwelling intensity, warmer sea surface temperature, and lower salinity (Ishii et al., 2014). Compared to the open EP, the efflux density of the coastal regions ($-0.334 \pm 0.071\ \mathrm{molC\,m^{-2}yr^{-1}}$) is roughly half that of the open ocean.

The South Pacific (SP) ranks second as a sink region for CO_2 with a yearly net flux of $0.358 \pm 0.029\ \mathrm{PgC\,yr^{-1}}$, mostly contributed by the open ocean (Fig. 6a). Uptake rates per unit area are very similar to those obtained for the SA (Fig. 6b). A detailed assessment reveals the open ocean influx density to be slightly lower ($0.791 \pm 0.066\ \mathrm{molC\,m^{-2}yr^{-1}}$), respectively the coastal one to be slightly higher ($0.987 \pm 0.063\ \mathrm{molC\,m^{-2}yr^{-1}}$) over the SP compared to the SA. Due to the larger area of the SP (Table 1), its integrated sink is approximately twice that of the SA. Similar to the processes discussed above for the SA, vertical mixing drives the uptake of CO_2 during austral winter (Takahashi et al., 2009; Ishii et al., 2014) and the effect of warming on CO_2 solubility during spring and summer is off-set by biological production. The latter leads to moderate to high uptake of CO_2 over the coasts and the southwest open sea (e.g., Eastern Australian Currents, Southern Australia, New Zealand) (Fig. 8). The influx density decreases eastward under the influence of the strong upwelling of DIC driven by the Peru Current.

https://doi.org/10.5194/bg-2021-207
Preprint. Discussion started: 3 August 2021

3.2.4 Indian Ocean

The total integrated Indian Ocean (IO) sink is evaluated to $0.300 \pm 0.033\ \mathrm{PgC\,yr^{-1}}$, with $0.305 \pm 0.033\ \mathrm{PgC\,yr^{-1}}$ contributed by the open ocean and a weak coastal source of $-0.004 \pm 0.002\ \mathrm{PgC\,yr^{-1}}$. The spatial distribution of flux densities (Fig. 5b) reveals the northwestern IO to be a net source of CO_2 to the atmosphere, while the northeastern IO is close to neutral and latitudes south of $18°S$ act as a strong sink. This regional compensation leads to a small open ocean influx density per unit area of $0.482 \pm 0.052\ \mathrm{molC\,m^{-2}yr^{-1}}$ and a small coastal efflux per unit area of $-0.131 \pm 0.061\ \mathrm{molC\,m^{-2}yr^{-1}}$ (Fig. 6b). The northern IO is a strong source of CO_2 sustained by the monsoon-driven seasonal upwelling along the Arabian and Somalian coasts (Behrenfeld et al., 2006; Sarma et al., 2013). The northeastern IO regions including the Bay of Bengal and its continental shelves receive fresh waters discharged from the Ganges river and lateral inputs from Indonesian outflows (see Sarma et al., 2013, and references therein), and switch between mild sources and sinks (Fig. 8). The Subtropical Front ($40°S$) divides the region south of $18°S$ into a weak sink to the North and over the oligotrophic gyre and a band of vigorous uptake to its South over the Subantarctic zone (SAZ) between $40°S$ and $44°S$ (Fig. 5b). Similar to the SA and SP, this entire region is identified as a significant net sink of CO_2 in winter (Fig. 8) possibly driven by enhanced solubility in response to cooling and mixing. While biological production maintains the sink over the SAZ during austral spring and summer months, warming reduces CO_2 uptake over the oligotrophic gyre.

3.2.5 Southern Ocean

The total Southern Ocean (SO) sink amounts to $0.349 \pm 0.070\ \mathrm{PgC\,yr^{-1}}$, including a coastal uptake of $0.018 \pm 0.002\ \mathrm{PgC\,yr^{-1}}$. The mean influx per unit area over the open SO is $0.468 \pm 0.104\ \mathrm{molC\,m^{-2}yr^{-1}}$ and close to the one obtained for the open IO (Fig. 6b). The area-averaged CO_2 drawdown over the coastal SO is $0.599 \pm 0.089\ \mathrm{molC\,m^{-2}yr^{-1}}$ with strong coastal sinks distributed over the South American and Antarctic shelves ($60°W$ westward as seen in Fig. 5b or S4b). During the austral spring and summer, intense phytoplankton blooms enhance the consumption of CO_2 over the Subantarctic and the Polar Frontal Zones between $44°$S and $58°$S (Sigman and Hain, 2012; Lenton et al., 2013), leading to a large sink with a flux density exceeding $1.667\ \mathrm{molC\,m^{-2}yr^{-1}}$ (Fig. 8). South of $58°$S, sea–ice retreat and vertical stratification contribute to a mild sink over the Antarctic Zone. During winter, vertical mixing brings DIC rich deep waters to the surface triggering a strong outgassing of CO_2 along the Antarctic Circumpolar Current.

4 Discussion

4.1 Contemporary air–sea CO_2 flux estimates

Our estimates of contemporary net fluxes of CO_2 for the global ocean and 11 open ocean regions are compared to estimates from RECCAP1 in Table 2 after adjusting them to the same period (1990–2009). RECCAP1 best estimates were derived from averages or medians of estimates based on the pCO_2 climatology or pCO_2 diagnostic model, and/or the atmospheric and ocean inversions and GOBM models (see Schuster et al., 2013; Ishii et al., 2014; Sarma et al., 2013; Lenton et al., 2013, and references

https://doi.org/10.5194/bg-2021-207
Preprint. Discussion started: 3 August 2021

therein). The observation-based estimates of regional net fluxes reported in these studies were computed from the reconstruction of SOCAT pCO_2 data (only used in Schuster et al., 2013), LDEO data (https://www.ldeo.columbia.edu/res/pi/CO2/), and its climatology (Takahashi et al., 2009). With the exception of the global ocean, coastal fluxes were not part of the earlier assessment. The global open ocean uptake obtained in this study of 1.344 ± 0.111 $\mathrm{PgC\,yr^{-1}}$ lies between the observation-based net sink estimate by Wanninkhof et al. (2013) (1.18 $\mathrm{PgC\,yr^{-1}}$) and the global sum of regional best estimates given in Table 2 (1.8 $\mathrm{PgC\,yr^{-1}}$). Net regional fluxes computed from CMEMS-LSCE-FFNN are mostly within the range of fluxes derived from observation-based reconstructions and multi-approach best estimates . Our Southern Ocean open ocean sink (0.290 ± 0.061 $\mathrm{PgC\,yr^{-1}}$) compares well with previous observation-based estimates (0.27 ± 0.13 $\mathrm{PgC\,yr^{-1}}$), but is lower than multi-approach best estimates (0.42 ± 0.07 $\mathrm{PgC\,yr^{-1}}$). A significant discrepancy between the present and previous estimates is also found over the Arctic ocean for which the regional open ocean net CO_2 uptake is about 1 order of magnitude lower in CMEMS-LSCE-FFNN compared to the RECCAP1 best estimate (Schuster et al., 2013).

Based on the MARCATS mask (Fig. 2), the CMEMS-LSCE-FFNN estimate of the yearly net coastal sink over the full reconstruction period is 0.150 ± 0.010 $\mathrm{PgC\,yr^{-1}}$. For 1990–2011, we estimate a yearly net coastal sink of 0.147 ± 0.009 $\mathrm{PgC\,yr^{-1}}$ which is lower than the one based on SOCATv2 data by Laruelle et al. (2014) (0.19 ± 0.05 $\mathrm{PgC\,yr^{-1}}$). Despite the fact that the present estimate was obtained with a model at a lower spatial resolution, the flux density of coastal sources and sinks, as well as their spatial distribution (Fig. S4b) are, in general, consistent with Laruelle et al. (2014) (Fig. 2) with exceptions found in Northern polar and subpolar regions. For instance, Laruelle et al. (2014) suggested the Okhotsk shelf to be a strong source of CO_2 in excess of -3 $\mathrm{molC\,m^{-2}yr^{-1}}$. To the contrary and in line with Otsuki et al. (2003), it is identified as a significant sink in this study taking up 1 to 2.333 $\mathrm{molC\,m^{-2}yr^{-1}}$ (Fig. 5).

Our estimates for the mean annual open and coastal ocean uptake over the Arctic ($> 76°N$) are 0.015 ± 0.001 $\mathrm{PgC\,yr^{-1}}$ and 0.010 ± 0.001 $\mathrm{PgC\,yr^{-1}}$ (Table 2) which are respectively less than the best estimate of 0.12 ± 0.06 $\mathrm{PgC\ yr^{-1}}$ by Schuster et al. (2013) and that of 0.07 $\mathrm{PgC\ yr^{-1}}$ by Laruelle et al. (2014). The discrepancy is possibly due to an overestimation of Arctic pCO_2 by the CMEMS-LSCE-FFNN (see in Sect. 3.1.2) and to the lack of estimates over a large portion of the seasonally sea–ice covered regions (see in Figs. 5 and 8). Further improvements would include using additional products of sea surface height and input from river discharge and sea–ice melt available over the Arctic. Besides, in Eq. (1), the air–sea flux density is a linear function of the sea–ice fraction leading to $fgCO_2 = 0$ as $f_{\mathrm{ice}} = 1$. Loose et al. (2009) suggest that the flux density in such regions is larger than evaluated by Eq. (1). A suggestion for a better assessment of air–sea fluxes over the Arctic and other regions with sea–ice cover (i.e., Antarctic and partly subpolar regions) would be to impose a sea–ice concentration of 99% for values exceeding 99% (Bates et al., 2006).

4.2 Model errors and uncertainties

Our uncertainty evaluation for estimates of pCO_2 and air–sea CO_2 fluxes is based on a Monte Carlo approach. Statistics (i.e., ensemble standard deviation) are based on ensembles of CMEMS-LSCE-FFNN model realizations. It allows producing spatially and temporally varying uncertainty fields of pCO_2 and $fgCO_2$ estimates covering the global ocean and the full period.

https://doi.org/10.5194/bg-2021-207
Preprint. Discussion started: 3 August 2021

This asset can be used for quantifying the uncertainty for different spatial and temporal resolutions (e.g., monthly/yearly integrated fluxes at regional/global scales).

As a complement to Fig. 3 (bottom plots) which generally evaluates the reliability of model uncertainty estimates compared to model–observation misfit deviations, Fig. 5 shows some similarity between their spatial distributions for pCO_2 (Figs. 5c and 5e) as for $fgCO_2$ (Figs. 5d and 5f). For pCO_2, large model–observation misfits and uncertainties are found over regions with sparse density or devoid of SOCAT data (see in Figs. S1a and S3), but also with high temporal and/or spatial pCO_2 variations (partly shown in Figs. S1b and S1c). High temporal/spatial gradients of pCO_2 are typically associated with upwelling systems (e.g., Eastern boundary upwelling systems, Arabian Sea upwelling), Western boundary currents (e.g., Gulf Stream, Kuroshio), intense biological production (e.g., spring bloom in temperate Northern/Southern latitudes), coastal and shelf dynamics including river runoff (e.g., Amazon, Congo, Mississippi, and great subpolar and Arctic rivers such as Ob, Yenisey, Lena, Mackenzie). Comparing between Figs. 5c and 5d (5e and 5f), the magnitude of the uncertainty estimates (model errors) of air–sea CO_2 flux estimates appears to be much less correlated to measurement density (Fig. S1) than the pCO_2 field (see also in Figs. 7a and 7b). The model uncertainty and errors of $fgCO_2$ estimates are highest over the open SO ($> 44°S$), the subpolar regions, the Indian gyre, and upwelling systems.

In this study, the uncertainty quantified for the reconstruction of pCO_2 and ultimately $fgCO_2$ is a result of randomly sampling training and validation datasets from predictors and SOCAT observations for 100 FFNN model runs (see Sect. 2.2). This subsampling approach permits to take into account an assumption of uncertainties of predictors and SOCAT data, i.e., random errors exist through changes in the range between their sub-samples. For a better assessment of the reconstruction uncertainty, future studies should include realistic uncertainties of these data, and also of local (sub-)skin effects of temperature and salinity as suggested in Watson et al. (2020). Additional sources of uncertainty in the computation of air–sea fluxes are discussed by Wanninkhof (2014); Woolf et al. (2019); Fay et al. (2021). These studies have demonstrated the strong impact of different wind field products and model parameterizations on the gas transfer velocity k in Eq. (1) and the corresponding air–sea flux estimates. For instance, using the eight expressions for the parameterization of k proposed in Woolf et al. (2019) and references therein would inflate the uncertainty of the global mean annual uptake from 5% to 10%. However, it would not significantly impact the spatial distribution of uncertainty, but only its magnitude.

4.3 Quantification of the global ocean carbon sink

Table 3 presents the comparison of estimates between the CMEMS-LSCE-FFNN, an ensemble of data-based reconstruction approaches, and an ensemble of global ocean biogeochemical models (GOBMs) used in the Global Carbon Project (GCP, Friedlingstein et al., 2019, 2020; Hauck et al., 2020) for the reconstruction of air–sea CO_2 fluxes. The reconstructed CMEMS-LSCE-FFNN field covers approximately 88.9% of the total ocean area used by the GCP ($361.9 \times 10^6\,\mathrm{km}^2$). The annual contemporary uptake over the global ocean and the full period 1985–2019 was 1.643 ± 0.125 PgC yr^{-1} with a starting net influx of 0.784 ± 0.178 PgC yr^{-1}, a growth rate of $+0.062 \pm 0.006$ PgC yr^{-2}, and an interannual variability (temporal standard deviation) of 0.526 ± 0.022 PgC yr^{-1} (Fig. 9). The contemporary sink amounted to 2.301 ± 0.126 PgC yr^{-1} for the last decade (2010s) and 2.877 ± 0.154 PgC yr^{-1} in the year 2019 (Table 3). The long term positive trend of the global ocean carbon sink

https://doi.org/10.5194/bg-2021-207
Preprint. Discussion started: 3 August 2021

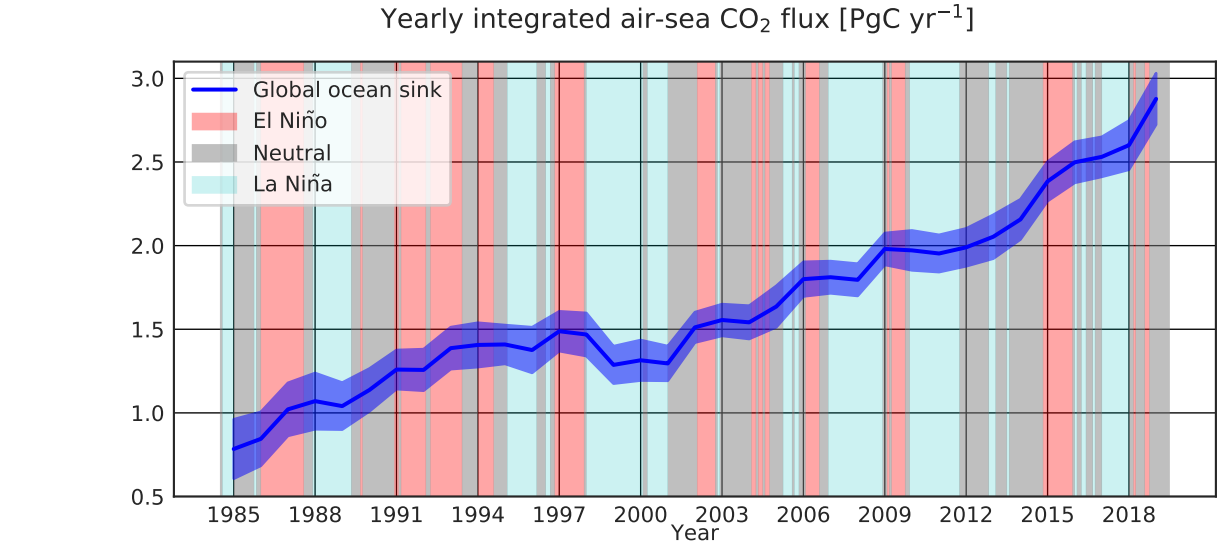

Figure 9. Yearly global integrated air–sea flux estimates derived from the CMEMS-LSCE-FFNN ensemble (mean ± uncertainty) for 1985–2019. Multivariate El Niño-Southern Oscillation Index (MEI; Wolter and Timlin, 1993, https://psl.noaa.gov/enso/mei/, last access: December 2020) is used to indicate a link between variations in the CMEMS-LSCE-FFNN sink estimate and the ENSO climate mode (El Niño: MEI $>$ 0.5, La Niña: MEI $<$ -0.5, Neutral: otherwise).

Table 3. Comparison of the global anthropogenic CO_2 uptake (mean ± uncertainty) between CMEMS-LSCE-FFNN, and data-based and model-based estimates used in the Global Carbon Project (Friedlingstein et al., 2019, 2020; Hauck et al., 2020). The CMEMS-LSCE-FFNN approach provides contemporary flux estimates. Anthropogenic flux estimates are derived from contemporary fluxes adjusted with the global ocean area of $361.9\times10^6\,km^2$ and the riverine flux of 0.78 PgC yr^{-1}. The estimates in parentheses were provided in Hauck et al. (2020) as the ensemble mean and standard deviation of the model- or data-based estimates.

		Periods					
Methods		1985–1989	1990–1999	2000–2009	2009–2018	2010–2019	2019
CMEMS	Contemporary	0.952 ± 0.162	1.347 ± 0.124	1.624 ± 0.103	2.212 ± 0.120	2.301 ± 0.126	2.877 ± 0.154
	Anthropogenic	1.757 ± 0.166	2.162 ± 0.127	2.446 ± 0.106	3.049 ± 0.123	3.141 ± 0.129	3.732 ± 0.158
GCP2019	Data		(2.32 ± 0.18)	(2.44 ± 0.14)	(3.09 ± 0.10)		
	Model		$2 \pm 0.6\,(1.99 \pm 0.25)$	$2.2 \pm 0.6\,(2.17 \pm 0.26)$	$2.5 \pm 0.6\,(2.52 \pm 0.29)$		
GCP2020	Model		2 ± 0.5	2.1 ± 0.5		2.5 ± 0.6	2.6 ± 0.6

estimates tracks the growth rate of atmospheric CO_2 concentration since the mid-1980s (Friedlingstein et al., 2019, 2020). The interanual to multi-annual variability of the global ocean carbon sink co-varies with cold and hot ENSO phases (Fig. 9) confirming ENSO as a leading mode of variability of the ocean carbon sink (Feely et al., 1999).

Taking into account the total ocean area of $361.9 \times 10^6\,km^2$ and the outgassing of river carbon of 0.78 PgC yr^{-1} (Resplandy et al., 2018) yields an anthropogenic sink estimate of 2.423 ± 0.125 PgC yr^{-1} for the years 1985–2019, respectively 3.141 ± 0.129 PgC yr^{-1} for the 2010s and 3.732 ± 0.158 PgC yr^{-1} for 2019. As shown in Table 3, the CMEMS-LSCE-FFNN estimates

https://doi.org/10.5194/bg-2021-207
Preprint. Discussion started: 3 August 2021

of the annual anthropogenic C uptake for different decades (1990s to 2010s) are in line with the data-based estimates but above the model-based estimates in the GCP publications. Hauck et al. (2020) demonstrated that the spatial distribution of CO_2 sources and sinks, as well as decadal trends of the annual mean flux estimates derived from the data-based reconstruction methods and the GOBMs are consistent at the global and regional scales. However, the mismatch in magnitude of these estimates, seasonal cycles, and their interannual variability are still large and remain to be resolved. Note that the uncertainties computed in Hauck et al. (2020) (see estimates in parentheses in Table 3) are defined as the ensemble standard deviation of multiple data-based or model-based products and are lower than the uncertainties reported in the GCP (Friedlingstein et al., 2019, 2020). The latter published a total estimate of ± 0.6 PgC yr^{-1} which corresponds to the combination of the interannual variability derived from GOBMs-based estimates (± 0.4 PgC yr^{-1}) and the uncertainty of the ensemble mean ocean sink ($\pm[0.2-0.4]$ PgC yr^{-1}).

5 Summary and Conclusions

In this paper, we proposed an ensemble of 100 feed-forward neural network models for the reconstruction of air–sea fluxes of CO_2 ($fgCO_2$) over the global ocean for the period 1985–2019. This *CMEMS-LSCE-FFNN* model was first used to reproduce the pCO_2 fields and we have evaluated its skill. The corresponding monthly fields of $fgCO_2$ were then deduced by applying the air–sea CO_2 flux formulation (Eq. 1). Mean state estimates and uncertainty from the CMEMS-LSCE-FFNN ensemble-based estimates of air–sea CO_2 fluxes have been analysed for the global ocean and 11 RECCAP1 sub-basins (Fig. 2) from the open seas to the continental shelves.

Our estimate for the contemporary net global sink over the period 1985–2019 is 1.643 ± 0.125 $\mathrm{PgC\,yr}^{-1}$ including 0.150 ± 0.010 $\mathrm{PgC\,yr}^{-1}$ for the coastal sink. The model suggested a net flux of 0.784 ± 0.178 $\mathrm{PgC\,yr}^{-1}$ in the year 1985 followed by an increase in the global ocean uptake with a growth rate of $+0.062 \pm 0.006$ $\mathrm{PgC\,yr}^{-2}$. CO_2 absorption by the ocean showed little fluctuation in the 1990s followed by an anomalous reduction in the years 1999–2001 (Fig. 9). Thereafter, the ocean sink has strengthened leading to a global uptake rate of 2.301 ± 0.126 $\mathrm{PgC\,yr}^{-1}$ in the 2010s. The large interannual to multi-year variations of the global carbon sink with a temporal standard deviation of 0.526 ± 0.022 PgC yr^{-1} are associated to the ENSO climate variability.

The global ocean sink and regional sources and sinks of CO_2 computed by CMEMS-LSCE-FFNN (Tables 2 and 3) were compared to the estimates by RECCAP1 (Canadell et al., 2011; Wanninkhof et al., 2013; Schuster et al., 2013; Ishii et al., 2014; Sarma et al., 2013; Lenton et al., 2013) and GCP (Friedlingstein et al., 2019; Hauck et al., 2020; Friedlingstein et al., 2020). We showed that the magnitude, spatial distribution, and seasonal variations of CMEMS-LSCE-FFNN CO_2 fluxes are generally consistent with those suggested in the preceding studies (Feely et al., 2001; Takahashi et al., 2009; Laruelle et al., 2014, 2017) for both the open and coastal seas. Mechanisms shaping the regional distribution (Figs. 5b and 6) and seasonal variations (Fig. 8) of net sinks and sources of CO_2 were briefly discussed in Sect. 3.2. The results in Fig. 6 also suggest a difference between the rank of 11 RECCAP1 sub-basins with respect to their total net sinks or sources and with respect to their mean flux densities per unit area:

https://doi.org/10.5194/bg-2021-207
Preprint. Discussion started: 3 August 2021

- Ranking regional contributions to the global integration of air-sea fluxes: the EP is confirmed as the predominant ocean source region compensating approximately 25% of the total sinks for both the open and coastal seas. The EA regions and the coastal IO are diagnosed as weak sources. Due to its large area, the open StP contributes with the largest regional sink of CO_2 to the global ocean net flux (the StP sink is equivalent to the EP source), followed by the SO, the IO, and the SP. For the coastal regions, the largest sink is computed for the SpA (one third of the total coastal uptake), followed by the northern Pacific and the SO.

- Ranking mean regional flux densities per unit area: the EP remains the strongest source of CO_2 followed by the EA and the coastal IO. The CO_2 absorption is higher over the Northern hemisphere than over the Southern one with the strongest uptake per unit area over the open Arctic and SpA. The coastal Arctic, SpA, and StP are identified as the dominant coastal sinks with similar flux densities.

Though statistics and relevant analyses throughout the paper have confirmed that the CMEMS-LSCE-FFNN estimates of sea surface pCO_2 and air–sea CO_2 fluxes are reasonably reliable, we believe that the model skill can be further improved. The spatial patterns of model–observation misfit (RMSD between SOCAT data and the reconstructed fields) and model uncertainty (ensemble standard deviation) computed by the proposed approach (Fig. 5) agree in pointing out where the model poorly recovers evaluation data and/or results large uncertainty estimates. We showed that the uncertainty fields (e.g., Figs. 5c and 5d) produced by the CMEMS-LSCE-FFNN approach are more informative than the standard error maps (e.g., Figs. 5e and 5f). Thus, the CMEMS-LSCE-FFNN uncertainty fields could be used to identify regions that should be prioritized in future extensions of the observational network and confirmed through dedicated observing system simulation experiments (Denvil-Sommer et al., 2021).

Data availability. The dataset of sea surface pCO_2 and air–sea CO_2 fluxes analysed in this study is available at https://resources.marine.copernicus.eu/?option=com_csw&view=details&product_id=MULTIOBS_GLO_BIO_CARBON_SURFACE_REP_015_008.

Author contributions. TTTC, MG, and FC developed the CMEMS-LSCE-FFNN model. TTTC conducted numerical experiments and analysed results with supports from MG and FC. All the authors contributed in preparing and completing the manuscript.

Competing interests. The authors declare that they have no conflict of interest.

Acknowledgements. The authors acknowledge funding from the European Copernicus Marine Environment Monitoring Service (CMEMS) for the MOB-TAC project in 2018–2021 (83-CMEMS-TAC-MOB contract, https://marine.copernicus.eu/about/producers/mob-tac).

https://doi.org/10.5194/bg-2021-207
Preprint. Discussion started: 3 August 2021

References

Arrigo, K. R., Pabi, S., van Dijken, G. L., and Maslowski, W.: air–sea flux of CO_2 in the Arctic Ocean, 1998–2003, J. Geophys. Res. Biogeosci., 115, https://doi.org/10.1029/2009JG001224, 2010.

Babin, M., Bélanger, S., Ellingsen, I., Forest, A., Le Fouest, V., Lacour, T., Ardyna, M., and Slagstad, D.: Estimation of primary production in the Arctic Ocean using ocean colour remote sensing and coupled physical–biological models: strengths, limitations and how they compare, Prog. Oceanogr., 139, 197–220, https://doi.org/10.1016/j.pocean.2015.08.008, 2015b.

Bakker, D. C. E., Pfeil, B., Landa, C. S., Metzl, N., O'Brien, K. M., Olsen, A., Smith, K., Cosca, C., Harasawa, S., Jones, S. D., Nakaoka, S., Nojiri, Y., Schuster, U., Steinhoff, T., Sweeney, C., Takahashi, T., Tilbrook, B., Wada, C., Wanninkhof, R., Alin, S. R., Balestrini, C. F., Barbero, L., Bates, N. R., Bianchi, A. A., Bonou, F., Boutin, J., Bozec, Y., Burger, E. F., Cai, W.-J., Castle, R. D., Chen, L., Chierici, M., Currie, K., Evans, W., Featherstone, C., Feely, R. A., Fransson, A., Goyet, C., Greenwood, N., Gregor, L., Hankin, S., Hardman-Mountford, N. J., Harlay, J., Hauck, J., Hoppema, M., Humphreys, M. P., Hunt, C. W., Huss, B., Ibánhez, J. S. P., Johannessen, T., Keeling, R., Kitidis, V., Körtzinger, A., Kozyr, A., Krasakopoulou, E., Kuwata, A., Landschützer, P., Lauvset, S. K., Lefèvre, N., Lo Monaco, C., Manke, A., Mathis, J. T., Merlivat, L., Millero, F. J., Monteiro, P. M. S., Munro, D. R., Murata, A., Newberger, T., Omar, A. M., Ono, T., Paterson, K., Pearce, D., Pierrot, D., Robbins, L. L., Saito, S., Salisbury, J., Schlitzer, R., Schneider, B., Schweitzer, R., Sieger, R., Skjelvan, I., Sullivan, K. F., Sutherland, S. C., Sutton, A. J., Tadokoro, K., Telszewski, M., Tuma, M., van Heuven, S. M. A. C., Vandemark, D., Ward, B., Watson, A. J., and Xu, S.: A multi-decade record of high-quality fCO_2 data in version 3 of the Surface Ocean CO_2 Atlas (SOCAT), Earth Syst. Sci. Data, 8, 383–413, https://doi.org/10.5194/essd-8-383-2016, 2016.

Bates, N. and Mathis, J.: The Arctic Ocean marine carbon cycle: evaluation of air–sea CO_2 exchanges, ocean acidification impacts and potential feedbacks, Biogeosciences, 6, https://doi.org/10.5194/bg-6-2433-2009, 2009.

Bates, N. R., Moran, S. B., Hansell, D. A., and Mathis, J. T.: An increasing CO_2 sink in the Arctic Ocean due to sea–ice loss, Geophys. Res. Lett., 33, https://doi.org/10.1029/2006GL027028, 2006.

Behrenfeld, M. J., O'Malley, R. T., Siegel, D. A., McClain, C. R., Sarmiento, J. L., Feldman, G. C., Milligan, A. J., Falkowski, P. G., Letelier, R. M., and Boss, E. S.: Climate-driven trends in contemporary ocean productivity, Nature, 444, 752–755, https://doi.org/doi:10.1038/nature05317, 2006.

Bourgeois, T., Orr, J. C., Resplandy, L., Terhaar, J., Ethé, C., Gehlen, M., and Bopp, L.: Coastal-ocean uptake of anthropogenic carbon, Biogeosciences, 13, 4167, https://doi.org/10.5194/bg-13-4167-2016, 2016.

Bushinsky, S. M., Landschützer, P., Rödenbeck, C., Gray, A. R., Baker, D., Mazloff, M. R., Resplandy, L., Johnson, K. S., and Sarmiento, J. L.: Reassessing Southern Ocean air–sea CO_2 flux estimates with the addition of biogeochemical float observations, Global Biogeochem. Cycles, 33, 1370–1388, https://doi.org/10.1029/2019GB006176, 2019.

Canadell, J. G., Ciais, P., Gurney, K., Le Quéré, C., Piao, S., Raupach, M. R., and Sabine, C. L.: An international effort to quantify regional carbon fluxes, Eos, Transactions American Geophysical Union, 92, 81–82, https://doi.org/10.1029/2011EO100001, 2011.

Carvalho, A., Kerr, R., Mendes, C., Azevedo, J., and Tavano, V.: Phytoplankton strengthen CO_2 uptake in the South Atlantic Ocean, Prog. Oceanogr., p. 102476, https://doi.org/10.1016/j.pocean.2020.102476, 2020.

Chavez, F. P., Sevadjian, J., Wahl, C., Friederich, J., and Friederich, G. E.: Measurements of pCO_2 and pH from an autonomous surface vehicle in a coastal upwelling system, Deep Sea Res. 2 Top. Stud. Oceanogr., 151, 137–146, https://doi.org/10.1016/j.dsr2.2017.01.001, 2018.

https://doi.org/10.5194/bg-2021-207
Preprint. Discussion started: 3 August 2021

Denvil-Sommer, A., Gehlen, M., Vrac, M., and Mejia, C.: LSCE-FFNN-v1: a two-step neural network model for the reconstruction of surface ocean pCO_2 over the global ocean, Geosci. Model Dev., 12, 2091–2105, https://doi.org/10.5194/gmd-12-2091-2019, 2019.

Denvil-Sommer, A., Gehlen, M., and Vrac, M.: Observation System Simulation Experiments in the Atlantic Ocean for enhanced surface ocean pCO_2 reconstructions, Ocean Sci. Disc. , pp. 1–23, https://doi.org/10.5194/os-2021-17, 2021.

Fay, A. R., Gregor, L., Landschützer, P., McKinley, G. A., Gruber, N., Gehlen, M., Iida, Y., Laruelle, G. G., Rödenbeck, C., and Zeng, J.: Harmonization of global surface ocean pCO_2 mapped products and their flux calculations; an improved estimate of the ocean carbon sink, Earth Syst. Sci. Data Disc., pp. 1–32, https://doi.org/10.5194/essd-2021-16, 2021.

Feely, R. A., Wanninkhof, R., Takahashi, T., and Tans, P.: Influence of El Niño on the equatorial Pacific contribution to atmospheric CO_2 accumulation, Nature, 398, 597–601, https://doi.org/10.1126/science.aam5776, 1999.

Feely, R. A., Sabine, C. L., Takahashi, T., and Wanninkhof, R.: Uptake and storage of Carbon Dioxide in the ocean: the global CO_2 survey, Oceanography, 14, 18–32, https://doi.org/10.5670/oceanog.2001.03, 2001.

Feely, R. A., Sabine, C. L., Hernandez-Ayon, J. M., Ianson, D., and Hales, B.: Evidence for upwelling of corrosive" acidified" water onto the continental shelf, Science, 320, 1490–1492, https://doi.org/10.1126/science.1155676, 2008.

Friedlingstein, P., Jones, M. W., O'Sullivan, M., Andrew, R. M., Hauck, J., Peters, G. P., Peters, W., Pongratz, J., Sitch, S., Le Quéré, C., Bakker, D. C. E., Canadell, J. G., Ciais, P., Jackson, R. B., Anthoni, P., Barbero, L., Bastos, A., Bastrikov, V., Becker, M., Bopp, L., Buitenhuis, E., Chandra, N., Chevallier, F., Chini, L. P., Currie, K. I., Feely, R. A., Gehlen, M., Gilfillan, D., Gkritzalis, T., Goll, D. S., Gruber, N., Gutekunst, S., Harris, I., Haverd, V., Houghton, R. A., Hurtt, G., Ilyina, T., Jain, A. K., Joetzjer, E., Kaplan, J. O., Kato, E., Klein Goldewijk, K., Korsbakken, J. I., Landschützer, P., Lauvset, S. K., Lefèvre, N., Lenton, A., Lienert, S., Lombardozzi, D., Marland, G., McGuire, P. C., Melton, J. R., Metzl, N., Munro, D. R., Nabel, J. E. M. S., Nakaoka, S.-I., Neill, C., Omar, A. M., Ono, T., Peregon, A., Pierrot, D., Poulter, B., Rehder, G., Resplandy, L., Robertson, E., Rödenbeck, C., Séférian, R., Schwinger, J., Smith, N., Tans, P. P., Tian, H., Tilbrook, B., Tubiello, F. N., van der Werf, G. R., Wiltshire, A. J., and Zaehle, S.: Global Carbon Budget 2019, Earth Syst. Sci. Data, 11, 1783–1838, https://doi.org/10.5194/essd-11-1783-2019, 2019.

Friedlingstein, P., O'Sullivan, M., Jones, M. W., Andrew, R. M., Hauck, J., Olsen, A., Peters, G. P., Peters, W., Pongratz, J., Sitch, S., Le Quéré, C., Canadell, J. G., Ciais, P., Jackson, R. B., Alin, S., Aragão, L. E. O. C., Arneth, A., Arora, V., Bates, N. R., Becker, M., Benoit-Cattin, A., Bittig, H. C., Bopp, L., Bultan, S., Chandra, N., Chevallier, F., Chini, L. P., Evans, W., Florentie, L., Forster, P. M., Gasser, T., Gehlen, M., Gilfillan, D., Gkritzalis, T., Gregor, L., Gruber, N., Harris, I., Hartung, K., Haverd, V., Houghton, R. A., Ilyina, T., Jain, A. K., Joetzjer, E., Kadono, K., Kato, E., Kitidis, V., Korsbakken, J. I., Landschützer, P., Lefèvre, N., Lenton, A., Lienert, S., Liu, Z., Lombardozzi, D., Marland, G., Metzl, N., Munro, D. R., Nabel, J. E. M. S., Nakaoka, S.-I., Niwa, Y., O'Brien, K., Ono, T., Palmer, P. I., Pierrot, D., Poulter, B., Resplandy, L., Robertson, E., Rödenbeck, C., Schwinger, J., Séférian, R., Skjelvan, I., Smith, A. J. P., Sutton, A. J., Tanhua, T., Tans, P. P., Tian, H., Tilbrook, B., van der Werf, G., Vuichard, N., Walker, A. P., Wanninkhof, R., Watson, A. J., Willis, D., Wiltshire, A. J., Yuan, W., Yue, X., and Zaehle, S.: Global Carbon Budget 2020, Earth Syst. Sci. Data, 12, 3269–3340, https://doi.org/10.5194/essd-12-3269-2020, 2020.

Gregor, L., Kok, S., and Monteiro, P. M. S.: Empirical methods for the estimation of Southern Ocean CO_2: support vector and random forest regression, Biogeosciences, 14, 5551–5569, https://doi.org/10.5194/bg-14-5551-2017, 2017.

Gregor, L., Kok, S., and Monteiro, P. M. S.: Interannual drivers of the seasonal cycle of CO_2 in the Southern Ocean, Biogeosciences, 15, 2361–2378, https://doi.org/10.5194/bg-15-2361-2018, 2018.

https://doi.org/10.5194/bg-2021-207
Preprint. Discussion started: 3 August 2021

Gregor, L., Lebehot, A. D., Kok, S., and Scheel Monteiro, P. M.: A comparative assessment of the uncertainties of global surface ocean CO_2 estimates using a machine-learning ensemble (CSIR-ML6 version 2019a) – have we hit the wall?, Geosci. Model Dev., 12, 5113–5136, https://doi.org/10.5194/gmd-12-5113-2019, 2019.

Gruber, N., Landschützer, P., and Lovenduski, N. S.: The variable Southern Ocean carbon sink, Ann. Rev. Mar. Sci., 11, 159–186, https://doi.org/10.1146/annurev-marine-121916-063407, 2019.

Hauck, J., Zeising, M., Le Quéré, C., Gruber, N., Bakker, D. C. E., Bopp, L., Chau, T. T. T., Gürses, z., Ilyina, T., Landschützer, P., Lenton, A., Resplandy, L., Rödenbeck, C., Schwinger, J., and Séférian, R.: Consistency and Challenges in the Ocean Carbon Sink Estimate for the Global Carbon Budget, Front. Mar. Sci., 7, 852, https://doi.org/10.3389/fmars.2020.571720, 2020.

Ibánhez, J. S. P., Diverrès, D., Araujo, M., and Lefèvre, N.: Seasonal and interannual variability of sea-air CO_2 fluxes in the tropical Atlantic affected by the Amazon River plume, Global Biogeochem. Cycles, 29, 1640–1655, https://doi.org/10.1002/2015GB005110, 2015.

Ishii, M., Feely, R. A., Rodgers, K. B., Park, G.-H., Wanninkhof, R., Sasano, D., Sugimoto, H., Cosca, C. E., Nakaoka, S., Telszewski, M., Nojiri, Y., Mikaloff Fletcher, S. E., Niwa, Y., Patra, P. K., Valsala, V., Nakano, H., Lima, I., Doney, S. C., Buitenhuis, E. T., Aumont, O., Dunne, J. P., Lenton, A., and Takahashi, T.: Air–sea CO_2 flux in the Pacific Ocean for the period 1990–2009, Biogeosciences, 11, 709–734, https://doi.org/10.5194/bg-11-709-2014, 2014.

Jamet, C., Moulin, C., and Lefèvre, N.: Estimation of the oceanic pCO_2 in the North Atlantic from VOS lines in situ measurements: parameters needed to generate seasonally mean maps, Ann. Geophys., 25, 2247–2257, https://doi.org/10.5194/angeo-25-2247-2007, 2007.

Kealoha, A. K., Shamberger, K. E., DiMarco, S. F., Thyng, K. M., Hetland, R. D., Manzello, D. P., Slowey, N. C., and Enochs, I. C.: Surface Water CO_2 variability in the Gulf of Mexico (1996–2017), Sci. Rep., 10, 1–13, https://doi.org/10.1038/s41598-020-68924-0, 2020.

Landschützer, P., Gruber, N., Bakker, D. C., Schuster, U., Nakaoka, S. I., Payne, M. R., Sasse, T. P., and Zeng, J.: A neural network-based estimate of the seasonal to interannual variability of the Atlantic Ocean carbon sink, Biogeosciences, 10, 7793–7815, https://doi.org/10.5194/bg-10-7793-2013, 2013.

Landschützer, P., Gruber, N., Bakker, D., and Schuster, U.: Recent variability of the global ocean carbon sink, Global Biogeochem. Cycles, 28, 927–949, https://doi.org/10.1002/2014GB004853, 2014.

Landschützer, P., Gruber, N., and Bakker, D. C.: Decadal variations and trends of the global ocean carbon sink, Global Biogeochem. Cycles, 30, 1396–1417, https://doi.org/10.1002/2015GB005359, 2016.

Landschützer, P., Ilyina, T., and Lovenduski, N. S.: Detecting regional modes of variability in observation-based surface ocean pCO_2, Geophys. Res. Lett., 46, 2670–2679, https://doi.org/10.1029/2018GL081756, 2019.

Landschützer, P., Laruelle, G. G., Roobaert, A., and Regnier, P.: A uniform pCO_2 climatology combining open and coastal oceans, Earth Syst. Sci. Data, 12, 2537–2553, https://doi.org/10.5194/essd-12-2537-2020, 2020.

Laruelle, G. G., Dürr, H., Lauerwald, R., Hartmann, J., Slomp, C., Goossens, N., and Regnier, P.: Global multi-scale segmentation of continental and coastal waters from the watersheds to the continental margins, Hydrol. Earth Syst. Sci., 17, 2029–2051, https://doi.org/10.5194/hess-17-2029-2013, 2013.

Laruelle, G. G., Lauerwald, R., Pfeil, B., and Regnier, P.: Regionalized global budget of the CO_2 exchange at the air-water interface in continental shelf seas, Global biogeochem. Cycles, 28, 1199–1214, https://doi.org/10.1002/2014GB004832, 2014.

Laruelle, G. G., Landschützer, P., Gruber, N., Tison, J.-L., Delille, B., and Regnier, P.: Global high-resolution monthly pCO_2 climatology for the coastal ocean derived from neural network interpolation, Biogeosciences, 14, 4545–4561, https://doi.org/10.5194/bg-14-4545-2017, 2017.

https://doi.org/10.5194/bg-2021-207
Preprint. Discussion started: 3 August 2021

Lenton, A., Tilbrook, B., Law, R. M., Bakker, D., Doney, S. C., Gruber, N., Ishii, M., Hoppema, M., Lovenduski, N. S., Matear, R. J., McNeil, B. I., Metzl, N., Mikaloff Fletcher, S. E., Monteiro, P. M. S., Rödenbeck, C., Sweeney, C., and Takahashi, T.: Sea–air CO_2 fluxes in the Southern Ocean for the period 1990-2009, Biogeosciences, 10, 4037–4054, https://doi.org/10.5194/bg-10-4037-2013, 2013.

Liu, K.-K., Kang, C.-K., Kobari, T., Liu, H., Rabouille, C., and Fennel, K.: Biogeochemistry and ecosystems of continental margins in the western North Pacific Ocean and their interactions and responses to external forcing–an overview and synthesis, Biogeosciences, 11, 7061–7075, https://doi.org/0.5194/bg-11-7061-2014, 2014.

Loose, B., McGillis, W., Schlosser, P., Perovich, D., and Takahashi, T.: Effects of freezing, growth, and ice cover on gas transport processes in laboratory seawater experiments, Geophys. Res. Lett., 36, https://doi.org/10.1029/2008GL036318, 2009.

Maritorena, S., d'Andon, O. H. F., Mangin, A., and Siegel, D. A.: Merged satellite ocean color data products using a bio-optical model: Characteristics, benefits and issues, Remote Sens. Environ., 114, 1791–1804, https://doi.org/10.1016/j.rse.2010.04.002, 2010.

Medeiros, P. M., Seidel, M., Ward, N. D., Carpenter, E. J., Gomes, H. R., Niggemann, J., Krusche, A. V., Richey, J. E., Yager, P. L., and Dittmar, T.: Fate of the Amazon River dissolved organic matter in the tropical Atlantic Ocean, Global Biogeochem. Cycles, 29, 677–690, https://doi.org/10.1002/2015GB005115, 2015.

Olafsson, J., Olafsdottir, S. R., Takahashi, T., Danielsen, M., and Arnarson, T. S.: Enhancement of the North Atlantic CO_2 sink by Arctic Waters, Biogeosciences, 18, 1689–1701, https://doi.org/10.5194/bg-18-1689-2021, 2021.

Otsuki, A. S., Watanabe, S., and Tsunogai, S.: Absorption of atmospheric CO_2 and its transport to the intermediate layer in the Okhotsk Sea, J. Oceanogr., 59, 709–717, https://doi.org/10.1023/B:JOCE.0000009599.94380.30, 2003.

Resplandy, L., Keeling, R., Rödenbeck, C., Stephens, B., Khatiwala, S., Rodgers, K., Long, M., Bopp, L., and Tans, P.: Revision of global carbon fluxes based on a reassessment of oceanic and riverine carbon transport, Nat. Geosci., 11, 504–509, https://doi.org/10.1038/s41561-018-0151-3, 2018.

Rödenbeck, C., Keeling, R. F., Bakker, D. C., Metzl, N., Olsen, A., Sabine, C., and Heimann, M.: Global surface-ocean pCO_2 and sea–air CO_2 flux variability from an observation-driven ocean mixed-layer scheme, Ocean Sci., 9, 193–216, https://doi.org/10.5194/os-9-193-2013, 2013.

Rödenbeck, C., Bakker, D. C. E., Gruber, N., Iida, Y., Jacobson, A. R., Jones, S., Landschützer, P., Metzl, N., Nakaoka, S., Olsen, A., Park, G.-H., Peylin, P., Rodgers, K. B., Sasse, T. P., Schuster, U., Shutler, J. D., Valsala, V., Wanninkhof, R., and Zeng, J.: Data-based estimates of the ocean carbon sink variability – first results of the Surface Ocean pCO_2 Mapping intercomparison (SOCOM), Biogeosciences, 12, 7251–7278, https://doi.org/10.5194/bg-12-7251-2015, 2015.

Sabine, C. L., Key, R. M., Feely, R. A., and Greeley, D.: Inorganic carbon in the Indian Ocean: Distribution and dissolution processes, Global Biogeochem. Cycles, 16, 15–1, https://doi.org/10.1029/2002GB001869, 2002.

Sabine, C. L., Hankin, S., Koyuk, H., Bakker, D. C. E., Pfeil, B., Olsen, A., Metzl, N., Kozyr, A., Fassbender, A., Manke, A., Malczyk, J., Akl, J., Alin, S. R., Bellerby, R. G. J., Borges, A., Boutin, J., Brown, P. J., Cai, W.-J., Chavez, F. P., Chen, A., Cosca, C., Feely, R. A., González-Dávila, M., Goyet, C., Hardman-Mountford, N., Heinze, C., Hoppema, M., Hunt, C. W., Hydes, D., Ishii, M., Johannessen, T., Key, R. M., Körtzinger, A., Landschützer, P., Lauvset, S. K., Lefèvre, N., Lenton, A., Lourantou, A., Merlivat, L., Midorikawa, T., Mintrop, L., Miyazaki, C., Murata, A., Nakadate, A., Nakano, Y., Nakaoka, S., Nojiri, Y., Omar, A. M., Padin, X. A., Park, G.-H., Paterson, K., Perez, F. F., Pierrot, D., Poisson, A., Ríos, A. F., Salisbury, J., Santana-Casiano, J. M., Sarma, V. V. S. S., Schlitzer, R., Schneider, B., Schuster, U., Sieger, R., Skjelvan, I., Steinhoff, T., Suzuki, T., Takahashi, T., Tedesco, K., Telszewski, M., Thomas, H., Tilbrook, B., Vandemark, D., Veness, T., Watson, A. J., Weiss, R., Wong, C. S., and Yoshikawa-Inoue, H.: Surface Ocean CO_2 Atlas (SOCAT) gridded data products, Earth Syst. Sci. Data, 5, 145–153, https://doi.org/10.5194/essd-5-145-2013, 2013.

https://doi.org/10.5194/bg-2021-207
Preprint. Discussion started: 3 August 2021

Sarma, V. V. S. S., Lenton, A., Law, R. M., Metzl, N., Patra, P. K., Doney, S., Lima, I. D., Dlugokencky, E., Ramonet, M., and Valsala, V.: Sea–air CO_2 fluxes in the Indian Ocean between 1990 and 2009, Biogeosciences, 10, 7035–7052, https://doi.org/10.5194/bg-10-7035-2013, 2013.

Schuster, U., McKinley, G. A., Bates, N., Chevallier, F., Doney, S. C., Fay, A. R., González-Dávila, M., Gruber, N., Jones, S., Krijnen, J., Landschützer, P., Lefèvre, N., Manizza, M., Mathis, J., Metzl, N., Olsen, A., Rios, A. F., Rödenbeck, C., Santana-Casiano, J. M., Takahashi, T., Wanninkhof, R., and Watson, A. J.: An assessment of the Atlantic and Arctic sea–air CO_2 fluxes, 1990–2009, Biogeosciences, 10, 607–627, https://doi.org/10.5194/bg-10-607-2013, 2013.

Sigman, D. M. and Hain, M. P.: The biological productivity of the ocean, Nature Education Knowledge, 3, 1–16, 2012.

Takahashi, T., Sutherland, S. C., Wanninkhof, R., Sweeney, C., Feely, R. A., Chipman, D. W., Hales, B., Friederich, G., Chavez, F., Sabine, C., Watson, A., Bakker, D. C., Schuster, U., Metzl, N., Yoshikawa-Inoue, H., Ishii, M., Midorikawa, T., Nojiri, Y., Körtzinger, A., Steinhoff, T., Hoppema, M., Olafsson, J., Arnarson, T. S., Tilbrook, B., Johannessen, T., Olsen, A., Bellerby, R., Wong, C., Delille, B., Bates, N., and de Baar, H. J.: Climatological mean and decadal change in surface ocean pCO_2, and net sea–air CO_2 flux over the global oceans, Deep Sea Res. 2 Top. Stud. Oceanogr., 56, 554–577, https://doi.org/https://doi.org/10.1016/j.dsr2.2008.12.009, 2009.

Wanninkhof, R.: Relationship between wind speed and gas exchange over the ocean revisited, Limnol. Oceanogr. Methods, 12, 351–362, https://doi.org/10.4319/lom.2014.12.351, 2014.

Wanninkhof, R., Park, G.-H., Takahashi, T., Sweeney, C., Feely, R., Nojiri, Y., Gruber, N., Doney, S. C., McKinley, G. A., Lenton, A., Le Quéré, C., Heinze, C., Schwinger, J., Graven, H., and Khatiwala, S.: Global ocean carbon uptake: magnitude, variability and trends, Biogeosciences, 10, 1983–2000, https://doi.org/10.5194/bg-10-1983-2013, 2013.

Watson, A. J., Schuster, U., Shutler, J. D., Holding, T., Ashton, I. G., Landschützer, P., Woolf, D. K., and Goddijn-Murphy, L.: Revised estimates of ocean-atmosphere CO_2 flux are consistent with ocean carbon inventory, Nat. Commun., 11, 1–6, https://doi.org/10.1038/s41467-020-18203-3, 2020.

Weiss, R.: Carbon dioxide in water and seawater: the solubility of a non-ideal gas, Mar. Chem., 2, 203–215, https://doi.org/10.1016/0304-4203(74)90015-2, 1974.

Wolter, K. and Timlin, M. S.: Monitoring ENSO in COADS with a seasonally adjusted principal, in: Proceedings of the 17th Climate Diagnostics Workshop, Norman, OK, NOAA/NMC/CAC, NSSL, Oklahoma Clim. Survey, CIMMS and the School of Meteor., Univ. of Oklahoma, 52, vol. 57, 1993.

Woolf, D., Shutler, J., Goddijn-Murphy, L., Watson, A., Chapron, B., Nightingale, P., Donlon, C., Piskozub, J., Yelland, M., Ashton, I., Holding, T., Schuster, U., Girard-Ardhuin, F., Grouazel, A., Piolle, J.-F., Warren, M., Wrobel-Niedzwiecka, I., Land, P., Torres, R., Prytherch, J., Moat, B., Hanafin, J., Ardhuin, F., and Paul, F.: Key uncertainties in the recent air–sea flux of CO_2, Global Biogeochem. Cycles, 33, 1548–1563, https://doi.org/https://doi.org/10.1029/2018GB006041, 2019.

Yasunaka, S., Murata, A., Watanabe, E., Chierici, M., Fransson, A., van Heuven, S., Hoppema, M., Ishii, M., Johannessen, T., Kosugi, N., Lauvset, S. K., Mathis, J. T., Nishino, S., Omar, A. M., Olsen, A., Sasano, D., Takahashi, T., and Wanninkhof, R.: Mapping of the air–sea CO_2 flux in the Arctic Ocean and its adjacent seas: Basin-wide distribution and seasonal to interannual variability, Polar Sci., 10, 323–334, https://doi.org/https://doi.org/10.1016/j.polar.2016.03.006, 2016.